



Available online at [www.sciencedirect.com](http://www.sciencedirect.com)

**SciVerse ScienceDirect**

Nuclear Physics B (Proc. Suppl.) 228 (2012) 139–175

**NUCLEAR PHYSICS B  
PROCEEDINGS  
SUPPLEMENTS**

[www.elsevier.com/locate/npbps](http://www.elsevier.com/locate/npbps)

## The Renormalization Group in Nuclear Physics

R. J. Furnstahl

*Department of Physics, Ohio State University, Columbus, OH 43210, USA*

### Abstract

Modern techniques of the renormalization group (RG) combined with effective field theory (EFT) methods are revolutionizing nuclear many-body physics. In these lectures we will explore the motivation for RG in low-energy nuclear systems and its implementation in systems ranging from the deuteron to neutron stars, both formally and in practice. Flow equation approaches applied to Hamiltonians both in free space and in the medium will be emphasized. This is a conceptually simple technique to transform interactions to more perturbative and universal forms. An unavoidable complication for nuclear systems from both the EFT and flow equation perspective is the need to treat many-body forces and operators, so we will consider these aspects in some detail. We'll finish with a survey of current developments and open problems in nuclear RG.

**Keywords:** Renormalization group, nuclear structure, three-body forces

### 1. Overview

The topic of these lectures is the use of renormalization group (RG) methods in low-energy nuclear systems, which include the full range of atomic nuclei as well as astrophysical systems such as neutron stars. We will examine why the RG has become an increasingly useful tool for nuclear physics theory over the last ten years and consider how to apply RG technology both formally and in practice. Of particular emphasis will be flow equation approaches applied to Hamiltonians both in free space and in the medium, which are an accessible but powerful method to make nuclear physics computationally more like quantum chemistry. We will see how interactions are evolved to increasingly universal form and become more amenable to perturbative methods. A key element in nuclear systems is the role of many-body forces and operators; dealing with their evolution is an important on-going challenge.

The expected background for these lectures is a thorough knowledge of nonrelativistic quantum mechanics,

including scattering, the basics of quantum field theory, and linear algebra (it's all matrices!). We will not assume a knowledge of nuclear structure or reactions, or even many-body physics beyond Hartree-Fock. No advanced computing experience is assumed (although Mathematica or MATLAB knowledge will be very helpful in exploring simple RG examples).

By necessity, we will only scratch the surface in these lectures. For a thorough treatment of flow equations for many-body systems not including nuclei, see the book by Kehrein [1]. For more details on applications of flow-equation and similar renormalization group methods to low-energy nuclear physics, the review article [2] and references therein are recommended.

### 2. Atomic nuclear at low resolution via RG

#### 2.1. Goals and scope of low-energy nuclear physics

The playing field for low-energy nuclear physics is the table of the nuclides, shown in Fig. 1. There are several hundred stable nuclei (black squares) but also several thousand *unstable* nuclei are known through experimental measurements. The total number of nuclides is

Email address: [furnstahl.1@osu.edu](mailto:furnstahl.1@osu.edu) ()

still unknown (see the region marked “terra incognita”), with theoretical estimates suggesting it could be as high as ten thousand! These unstable nuclei are the object of scrutiny for new and planned experimental facilities around the world. The challenge for low-energy nuclear theory is to describe their structure and reactions. We’ll return in the final lecture to discuss the overlapping regions where the theoretical many-body methods listed in the figure can be applied.

Let’s start with some of the questions that drive low-energy nuclear physics research. These include general questions about the physics of nuclei [3]:

- How do protons and neutrons make stable nuclei and rare isotopes? Where are the limits?
- What is the equation of state of nucleonic matter?
- What is the origin of simple patterns observed in complex nuclei?
- How do we describe fission, fusion, and other nuclear reactions?

These topics inform and are in turn illuminated by applications to other fields, such as astrophysics, where one can ask:

- How did the elements from iron to uranium originate?
- How do stars explode?
- What is the nature of neutron star matter?

or of fundamental symmetries:

- Why is there now more matter than antimatter in the universe?
- What is the nature of the neutrinos, what are their masses, and how have they shaped the evolution of the universe?

Finally, there are applications, for which we are led to ask: How can our knowledge of nuclei and our ability to produce them benefit humankind? The impact is very broad, encompassing the Life Sciences, Material Sciences, Nuclear Energy, and National Security.

In Figure 2, the energy scales of nuclear physics are illustrated. There is an extended hierarchy, which is a challenge, but also an opportunity to make use of effective field theory (EFT) and renormalization group (RG) techniques. The ratio of scales can become an expansion parameter, leading to a systematic treatment at lower energies. The progression from top to bottom can

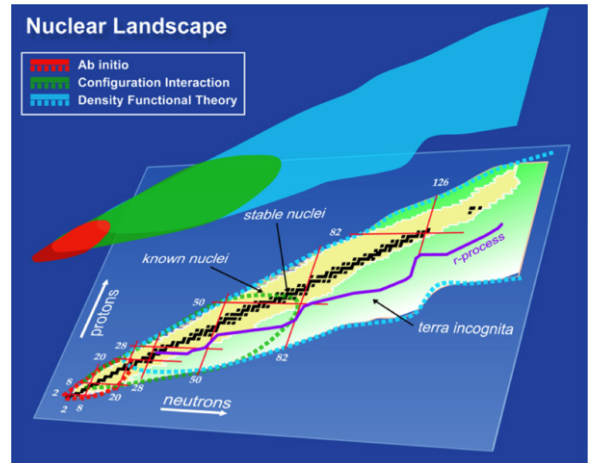


Figure 1: The nuclear landscape. A nuclide is specified by the number of protons and neutrons [3].

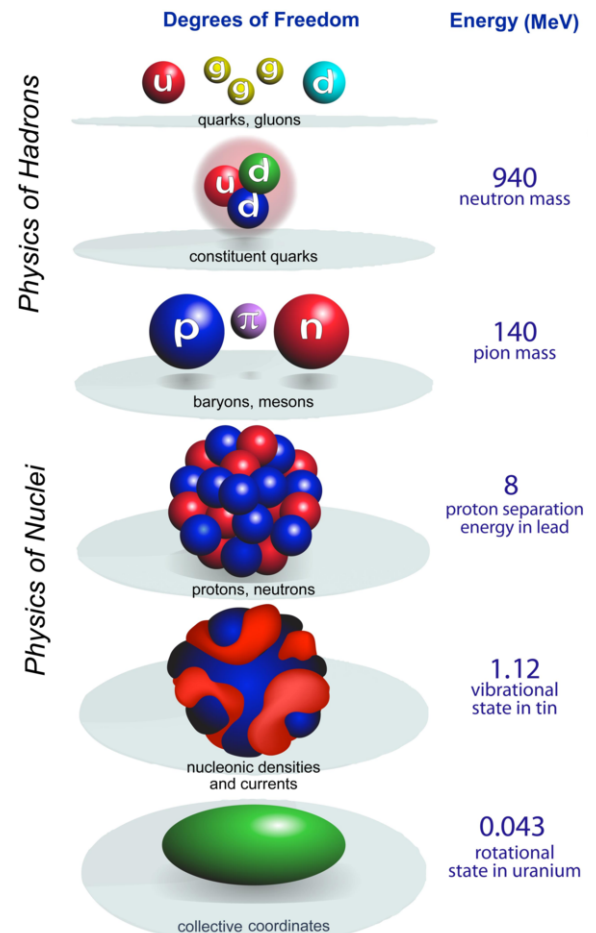


Figure 2: Hierarchy of nuclear degrees of freedom and associated energy scales [3].

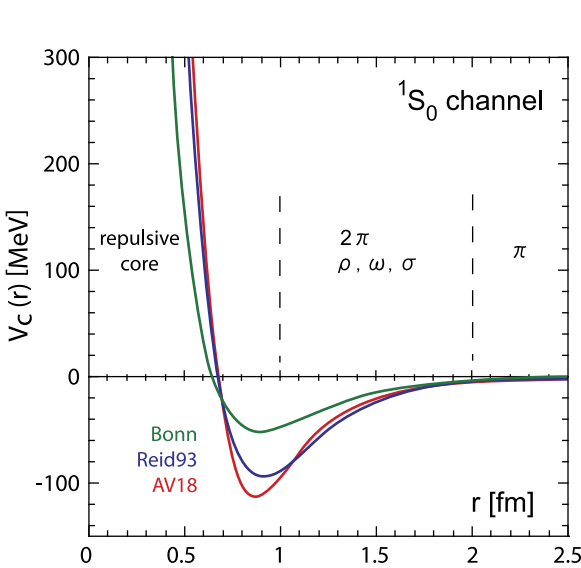


Figure 3: Some phenomenological potentials that accurately describe proton-neutron scattering up to laboratory energies of 300 MeV [4].

be viewed as a reduction in resolution. In these lectures, our focus is on the intermediate region only, where protons and neutrons are the relevant degrees of freedom. But even within this limited scope, the concept of reducing resolution by RG methods is extremely powerful.

## 2.2. Lowering the resolution with RG

What do we mean by resolution? Even the general public these days is familiar with the concept of digital resolution for computer screens, cellphones, televisions. High resolution is associated with more pixels, which follows because as pixel size becomes small compared to characteristic scales in an image, greater detail is seen. In our discussion, we associate resolution with the Fourier transform space and the phenomenon of diffraction.

Recall the basic physics: if the wavelength of light is comparable to or larger than an aperture, then diffraction is significant. If there are two sources, we say we can resolve them if the diffracted images don't overlap too much. For a fixed angle between sources or details in the object being observed, we find that the wavelength determines whether or not we resolve the details. Being unable to resolve details at long wavelength is generally considered to be a disadvantage (e.g., for astronomical observations), but we turn it to an advantage.

A fundamental principle of *any* effective low-energy description (not restricted to nuclear physics!) is that if a system is probed at low energies, fine details are

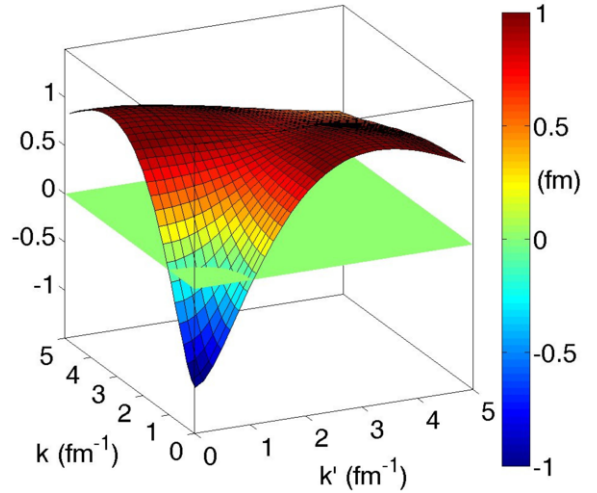


Figure 4: Momentum space representation of the Argonne  $v_{18}$  (AV18) NN potential in the  $^1S_0$  channel [2].

not resolved, and one can instead use low-energy variables for low-energy processes. Renormalization theory tells us that the short-distance structure can be replaced by something simpler without distorting low-energy *observables*. The familiar analog from classical electrodynamics is the replacement of a complicated charge or current distribution with a truncated multipole expansion. In the quantum case, the replacement can be done by constructing a model, or in a systematic way using effective field theory. We emphasize that while observable quantities (such as cross sections) do not change, the physics interpretation can (and generally does) change with resolution. What if there is no external probe? Then the particles still probe each other with resolution set by their de Broglie wavelengths. Low-density nuclear systems would seem to imply low resolution. But the picture is complicated by the nature of traditional internucleon potentials.

Figure 3 shows several phenomenological potentials that reproduce nucleon-nucleon scattering phase shifts up to about 300 MeV in lab energy. They are characterized by a long-range attractive tail from one-pion exchange, intermediate attraction, and a strongly repulsive short-range “core”. For our purposes, the partial-wave momentum-space representation, such as

$$\langle k | V_{L=0} | k' \rangle \propto \int r^2 dr j_0(kr) V(r) j_0(k'r) \quad (1)$$

for S-waves is more useful. Here  $k$  and  $k'$  are the relative momenta of the two nucleons. This is shown for the AV18 potential in Fig. 4 in the  $^1S_0$  channel. (The spin and isospin dependence of the nuclear interactions

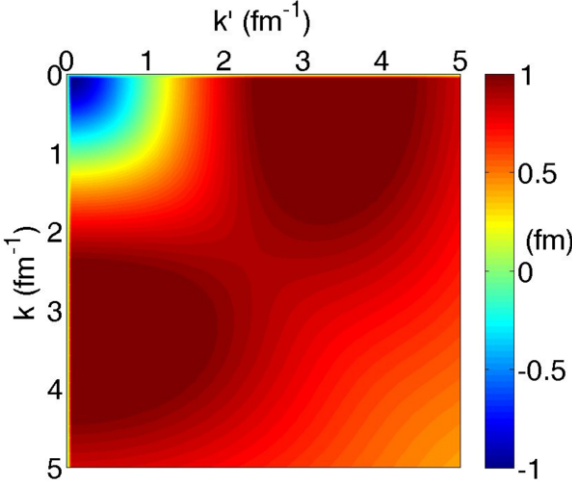


Figure 5: Alternative momentum space representation of the AV18 potential in the  $^1S_0$  channel [2].

is very important, unlike the situation in quantum chemistry.) In the momentum basis, the potentials in Fig. 3 are no longer diagonal, so we need three-dimensional information, but we generally use the flat contour representation of the same information, as in Fig. 5. The RG evolution of potentials will be visualized as changes in such pictures.

We work in units for which  $\hbar = c = 1$ . Then the typical relative momentum in the Fermi sea of any large nucleus is of order  $1 \text{ fm}^{-1}$  or  $200 \text{ MeV}$ . However, it is evident from Figs. 4 and 5 that there are large matrix elements connecting such momenta to much larger momenta. This is directly associated with the repulsive core of the potential. For our discussion, we will adopt  $2 \text{ fm}^{-1}$  as the (arbitrary but reasonable) dividing line between low and high momentum for nuclei.

The consequences of the coupling to high momentum are readily seen in the probability density of the only two-body bound state, the deuteron. Consider the Argonne  $v_{18}$  [5] curve in Fig. 6. The probability at small separations is significantly suppressed as a result of high-momentum components in the wave function. This suppression, called “short-range correlations” in this context, carries over to many-body wave functions and greatly complicates basis expansions. For example, in a harmonic oscillator basis, which is frequently the choice for self-bound nuclei because it readily allows removal of center-of-mass contamination, convergence is greatly slowed by the need to accommodate high-momentum components. The factorial growth of the basis size with the number of nucleons then greatly limits the reach of calculations.

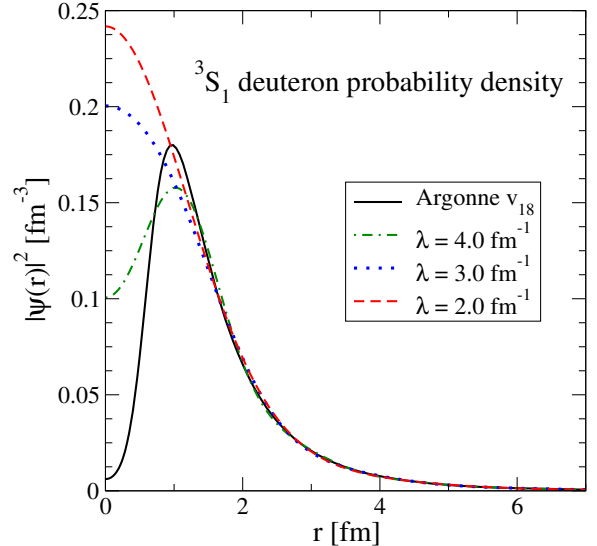


Figure 6: Short-range correlations in the deuteron  $^3S_1$  probability density from the AV18 potential (solid line). They are essentially eliminated by the RG evolution to lower flow parameter  $\lambda$  (see Section 3.1).

The underlying problem is that the resolution scale induced by the potential is mismatched with the basic scale of the low-energy nuclear states (given, for example, by the Fermi momentum). A solution is to eliminate the coupling to high momentum. This is readily accomplished for spatial images (i.e., photographs) by Fourier transforming and then applying a low-pass filter—simply set the short wavelength parts to zero—and then transforming back. Let’s try that for our Hamiltonian by setting to zero all of the matrix elements in Fig. 5 for  $k > 2 \text{ fm}^{-1}$ . We test the implications by seeing the effect on scattering phase shifts in the region of laboratory energies corresponding to  $k \leq 2 \text{ fm}^{-1}$ .

The result is shown in Fig. 7. It would be unsurprising that our filtered Hamiltonian fails close to the cut-off, but it is evident that there is a failure at all energies. What happened? The basic problem is that low momentum and high momentum are coupled when solving quantum mechanically for observables. For example, consider perturbation theory for the (tangent) of the phase shift (represented schematically here):

$$\langle k|V|k\rangle + \sum_{k'} \frac{\langle k|V|k'\rangle\langle k'|V|k\rangle}{(k^2 - k'^2)/m} + \dots \quad (2)$$

where a low momentum  $k$  is mixed with all other momenta at second order to a degree based on the size of the off-diagonal matrix elements. (As a computational aside, although momentum is continuous in principle, in practice we work on a discrete grid. This means that

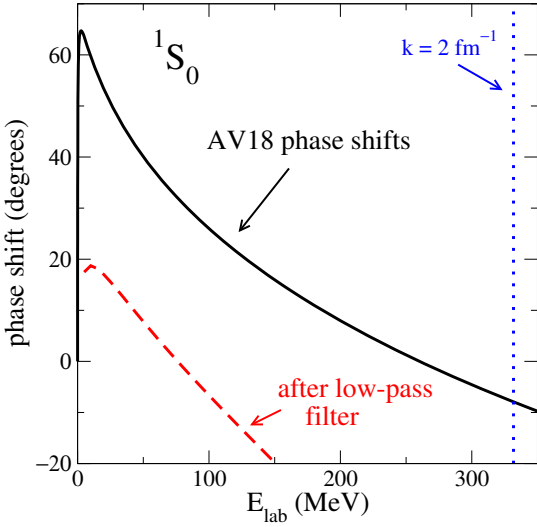


Figure 7: Effect of a low-pass filter on observables: the  $^1S_0$  phase shifts. Note that the AV18 phase shifts reproduce experimentally extracted phase shifts in this energy range.

Eq. (2) becomes a matrix equation. For two-body potentials, roughly  $100 \times 100$  matrices are sufficient.) The phase shift even at low energy or  $k$  will get large contributions from high  $k'$  if the coupling matrix elements  $\langle k|V|k' \rangle$  are large.

How can we fix this? Our solution is to use a (short-distance) unitary transformation of the Hamiltonian matrix to *decouple* low and high energies. That is, insert the operator  $U^\dagger U = 1$  repeatedly:

$$\begin{aligned} E_n &= \langle \Psi_n | H | \Psi_n \rangle = \langle \Psi_n | U^\dagger ) U H U^\dagger U | \Psi_n \rangle \\ &\equiv \langle \tilde{\Psi}_n | \tilde{H} | \tilde{\Psi}_n \rangle. \end{aligned} \quad (3)$$

In doing so we have modified operators *and* wavefunctions but observables (measurable quantities) are unchanged. An appropriate choice of the unitary transformation can, in principle, achieve the desired decoupling. This general approach has long been used in nuclear structure physics and for other many-body applications. The new feature here is the use of renormalization group flow equations to create the net unitary transformation via a series of infinitesimal transformations.

The renormalization group is well suited to this purpose. The common features of RG for critical phenomena and high-energy scattering are discussed by Steven Weinberg in an essay in Ref. [6]. He summarizes:

“The method in its most general form can I think be understood as a way to arrange in various theories that the degrees of freedom that you’re talking about are the relevant degrees of freedom for the problem at hand.”

This is the essence of what is done with the low-momentum interaction approaches considered here: arrange for the degrees of freedom for nuclear structure to be the relevant ones. This does not mean that other degrees of freedom cannot be used, but to again quote Weinberg [6]: “You can use any degrees of freedom you want, but if you use the wrong ones, you’ll be sorry.”

The consequences of using RG for high-energy (particle) physics include improving perturbation theory, e.g., in QCD. A mismatch of energy scales can generate large logarithms that ruins perturbative convergence even when couplings by themselves are small. The RG shifts strength between loop integrals and coupling constants to reduce these logs. For critical phenomena in condensed matter systems, the RG reveals the nature of observed universal behavior by filtering out short-distance degrees of freedom. We will see both these aspects in our calculations of nuclear structure and reactions. The end result can be said to make nuclear physics look more like quantum chemistry, opening the door to a wider variety of techniques (such as many-body perturbation theory) and simplifying calculations (e.g., by improving convergence of basis expansions).

### 2.3. Summary points

Low-energy nuclear physics is made difficult by a mismatch of energy scales inherent in conventional phenomenological potentials and those of nuclear structure and reactions. The renormalization group offers a way out by lowering the resolution, which means decoupling low- from high-momentum degrees of freedom.

## 3. Overview of flow equations

In Fig. 8, we show schematically two options for how the RG can be used to decouple a Hamiltonian matrix. The more conventional approach on the left in Fig. 8 lowers a cutoff  $\Lambda$  in momentum in small steps, with the matrix elements adjusted by requiring some quantity such as the on-shell T-matrix to be invariant. (In practice this may be carried out by enforcing that the half-on-shell T-matrix is independent of  $\Lambda$ .) Matrix elements above  $\Lambda$  are zero and are therefore trivially decoupled. When adapted to low-energy nuclear physics, this approach is typically referred to as “ $V_{\text{low } k}$ ” [7, 2].

The approach we will focus on is illustrated in Fig. 8 on the right, in which the matrix is driven toward band-diagonal form, achieving decoupling again but without truncating the matrix. The corresponding RG was developed in the early 1990’s by Wegner [8, 9, 10] for condensed matter applications under the name “flow equations” and independently by Glazek and Wilson [11] for

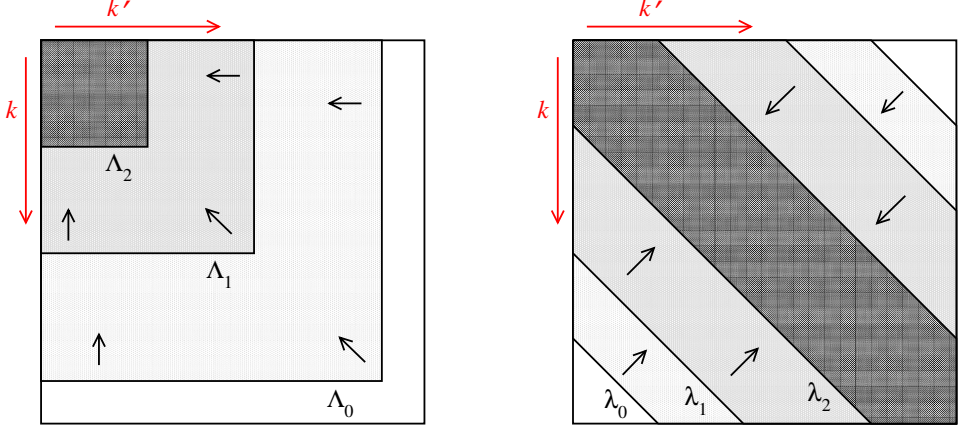


Figure 8: Schematic  $V_{\text{low } k}$  RG evolution (left) and flow equation RG evolution (right).

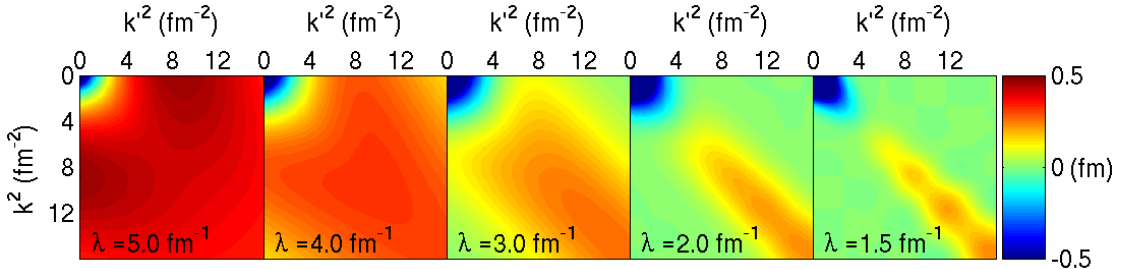


Figure 9: SRG flow of the AV18 NN potential in the  $^3S_1$  channel at selected values of the flow parameter  $\lambda$  [2].

solving quantum chromodynamics in light-front formalism under the name “similarity renormalization group” (SRG). Only in the last five years was it realized that the band-diagonal approach is particular well suited for low-energy nuclear physics, where it is technically simpler and more versatile than other methods [12, 2]. We will apply formalism closer to the flow equation formulation, but generally use the simple abbreviation SRG. We have introduced a cutoff-like parameter  $\lambda$  that serves as a momentum decoupling scale. Elsewhere we will also use the natural flow parameter  $s = 1/\lambda^4$ .

### 3.1. Flow equation basics

The basic flow equation is a set of coupled differential equations for the (discrete) matrix elements of the Hamiltonian matrix (or the potential in practice, because we fix the kinetic energy matrix by construction). Let’s see an example in action before stepping back and considering details. For the two-body potential in a partial-

wave momentum basis, the flow equation takes the form

$$\begin{aligned} \frac{dV_\lambda}{d\lambda}(k, k') &\propto -(\epsilon_k - \epsilon_{k'})^2 V_\lambda(k, k') \\ &+ \sum_q (\epsilon_k + \epsilon_{k'} - 2\epsilon_q) V_\lambda(k, q) V_\lambda(q, k'), \end{aligned} \quad (4)$$

where  $k$  and  $k'$  are the relative momenta and  $\epsilon_k \equiv \hbar^2 k^2/M$  and we have omitted an inessential constant. The evolution is continuous, but snapshots at selected  $\lambda$  values are shown in Fig. 9. (Note that the axes are the kinetic energy  $k^2$ .) The evolution toward diagonalization is evident, with the width of the band in  $k^2$  roughly given by  $\lambda^2$ .

It is evident that the off-diagonal matrix elements are driven toward zero, so we expect that a low pass filter will now be effective. Indeed it is, as shown in Fig. 10, where NN phase shifts for the AV18 potential in a variety of channels are compared with the results from applying a low-pass filter to the original (dotted) and evolved (dashed) potentials. The evolved result agrees up to the low-pass cutoff. Note that if this cutoff is not applied, the phase shifts for the evolved Hamiltonian

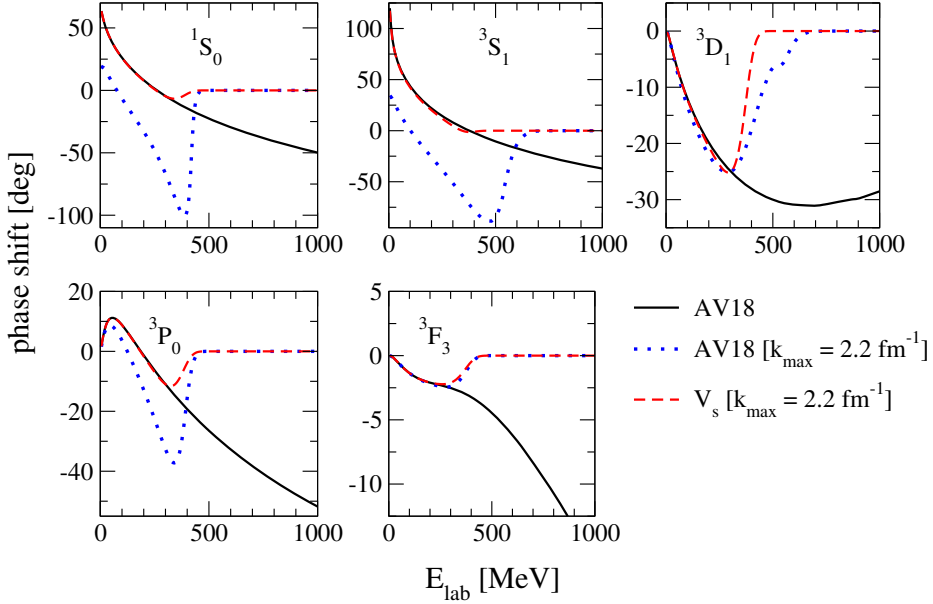


Figure 10: Nucleon-nucleon (NN) phase shifts showing the effect of a low-pass filter at  $k_{\max} = 2.2 \text{ fm}^{-1}$  in various partial-wave channels [13, 14]. In each panel, the solid line is for the original AV18 potential while the dotted line is the result when the potential is set to zero for  $\{k, k'\} > k_{\max}$ . The dashed line is the results when the potential is evolved first and then cut at  $k_{\max}$ .

agree precisely *at all energies*, because the transformation is unitary in the two-body system (and this is preserved to high numerical precision).

If we now revisit the consequence of a repulsive core for the deuteron probability density, we see in Fig. 6 that the “wound” in the wave function at small  $r$  is filled in as the core is transformed away. (Note: it may look like the normalization is not conserved, but if we multiplied by  $r^2$ , we would see that the area under the curves is the same, as are the large- $r$  tails.) Thus the short-range correlations in the wave function are drastically reduced. This means that the physics interpretation of various phenomena is altered, even though the observable quantities such as energies and cross sections are unchanged. (The long-range part of the wave function is preserved; this is related to the asymptotic normalization constants, which can be extracted from experiment.) We cannot immediately visualize the changes in the potential in coordinate space in a conventional plot like Fig. 3, however, because it is now *non-local*, which is to say it is not diagonal in coordinate representation:

$$V(\mathbf{r})\psi(\mathbf{r}) \longrightarrow \int d^3\mathbf{r}' V(\mathbf{r}, \mathbf{r}')\psi(\mathbf{r}'). \quad (5)$$

This is a technical problem for certain quantum many-body methods (such as Green’s function Monte Carlo) but not for methods using harmonic oscillator matrix el-

ements.

We can visualize the evolution *approximately* by considering a local projection of the potential:

$$\bar{V}_\lambda(r) = \int d^3\mathbf{r}' V_\lambda(r, \mathbf{r}') \quad (6)$$

which leaves a local  $V(r)$  unchanged. For a non-local potential, this roughly gives the action of the potential on long-wavelength nucleons. This is shown in Figs. 11 and 12, where in the former we see the central potential dissolving and in the latter similar effects on the tensor part of the potential [15]. Also evident is the flow of the two potentials, initially quite different (potentials are not observables!), toward a universal flow at the lower values of  $\lambda$ . Very recent work suggests that such a local projection may capture most of the physics of the full evolved potential, with the effects of the residual potential calculable in perturbation theory. This may open the door to using RG-evolved potential with quantum Monte Carlo methods.

The consequences of low-momentum potentials for harmonic-oscillator-basis calculations are illustrated in Figs. 13 and 14. (We’ll refer to the method used, which is a direct diagonalization of the Hamiltonian matrix and therefore is variational, as no-core full configuration, or NCFC.) The original potential in this case is already soft (that is, there is much less coupling to high mo-

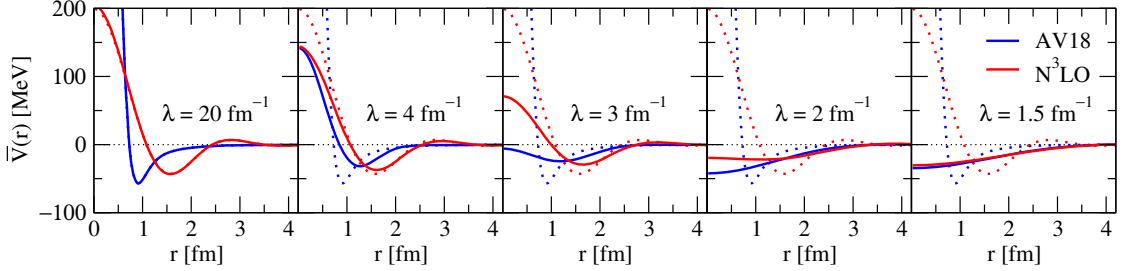


Figure 11: Local projection of AV18 and N3LO(500 MeV) potentials in  $^3S_1$  channel at different resolutions [15].

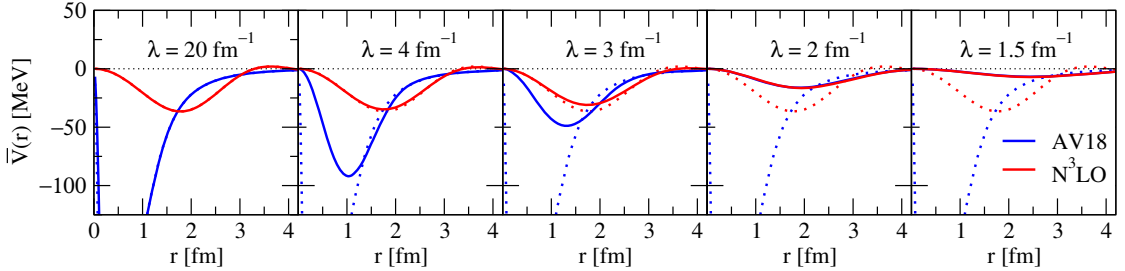


Figure 12: Local projection of AV18 and N3LO(500 MeV) potentials in mixed  $^3S_1$ – $^3D_1$  channel at different resolutions [15].

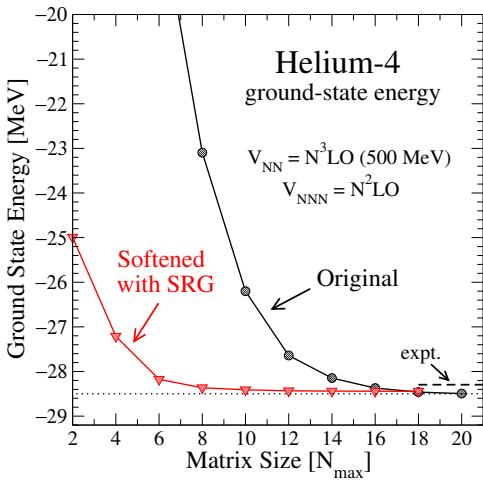


Figure 13: Convergence of NCFC calculations of the  $^4\text{He}$  ground state energy with basis size at SRG different resolutions. The initial potential includes both two- and three-body components [16, 17].

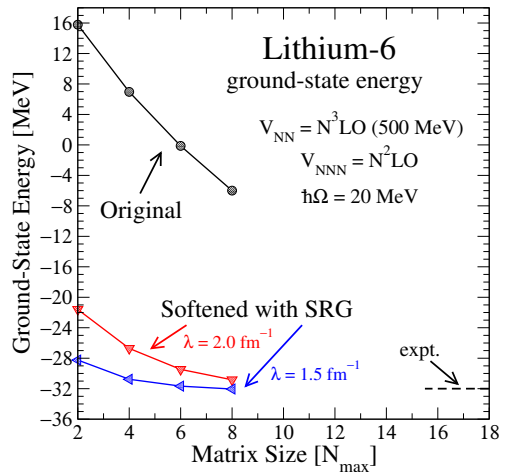


Figure 14: Convergence of NCFC calculations of the  $^6\text{Li}$  ground state energy with basis size at SRG different resolutions. The initial potential includes both two- and three-body components [16, 17].

momentum than in the AV18 potential), but convergence in a harmonic oscillator basis with  $N_{\max}$  shells for excitation is slow (these are the “Original” curves). Note that the matrix dimension grows rapidly with  $N_{\max}$  and the number of nucleons  $A$ ; for example  $N_{\max} = 8$  has dimension about 50,000 for  $^4\text{He}$  but over one million

for  $^6\text{Li}$  (see Fig. 15 for other examples). But with SRG evolution, there is vastly improved convergence. The convergence is also smooth, which makes it possible to reliably extrapolate partly converged results to the  $N_{\max} \rightarrow \infty$  limit. Nevertheless, the rapid growth of the basis with  $A$  is still a major hindrance to calculat-

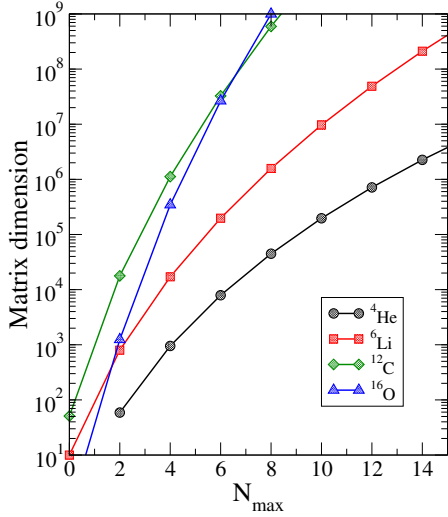


Figure 15: Dimension of the Hamiltonian matrix for NCFC/NCSM calculations as a function of the harmonic oscillator basis size ( $N_{\max}$ ) for selected nuclei.

ing larger nuclei. One solution being explored by Roth and collaborators [18, 19] is to use importance sampling of matrix elements, in which only a fraction of the full matrix is used. This technique is enabled by the RG softening of the potential, which allows the importance to be evaluated perturbatively.

Let's now return to the basics of SRG flow equations. We wish to transform an initial hamiltonian,  $H = T + V$  in a series of steps, labeled by the flow parameter  $s$ :

$$H_s = U_s H U_s^\dagger \equiv T + V_s \quad (7)$$

with

$$U_s^\dagger U_s = U_s U_s^\dagger = 1. \quad (8)$$

Note that the kinetic energy  $T$  is taken to be independent of  $s$ . Differentiating with respect to  $s$ :

$$\begin{aligned} \frac{dH_s}{ds} &= \frac{dU_s}{ds} U_s^\dagger U_s H U_s^\dagger + U_s H U_s^\dagger U_s \frac{dU_s^\dagger}{ds} \\ &= [\eta_s, H_s] \end{aligned} \quad (9)$$

with

$$\eta_s \equiv \frac{dU_s}{ds} U_s^\dagger = -\eta_s^\dagger. \quad (10)$$

The anti-Hermitian generator  $\eta_s$  can be specified by a commutator of  $H_s$  with a Hermitian operator  $G_s$ :

$$\eta_s = [G_s, H_s], \quad (11)$$

which yields the flow equation (with  $T$  held fixed!),

$$\frac{dH_s}{ds} = \frac{dV_s}{ds} = [[G_s, H_s], H_s]. \quad (12)$$

The operator  $G_s$  determines the flow and there are many choices one can consider.

Probably the simplest example we can consider is just a two-state system [20]. Let  $H = T + V$ , where

$$T|i\rangle = \epsilon_i |i\rangle \quad \text{and} \quad V_{ij} \equiv \langle i|V|j\rangle. \quad (13)$$

Then we can choose  $G_s = T$  and

$$\frac{dH_s}{ds} = [[T, H_s], H_s] \quad (14)$$

becomes (with the  $s$  dependence implicit)

$$\begin{aligned} \frac{d}{ds} V_{ij} &= -(\epsilon_i - \epsilon_j)^2 V_{ij} \\ &+ \sum_k (\epsilon_i + \epsilon_j - 2\epsilon_k) V_{ik} V_{kj}. \end{aligned} \quad (15)$$

For a two-level system with  $i = \{a, b\}$ , we can express the flowing Hamiltonian in terms of Pauli matrices:

$$T = \frac{1}{2}(\epsilon_a + \epsilon_b)I + \frac{1}{2}(\epsilon_a - \epsilon_b)\sigma_z \quad (16)$$

and

$$\begin{aligned} V_s &= \frac{1}{2}(V_{aa} + V_{bb})I \\ &+ \frac{1}{2}(V_{aa} - V_{bb})\sigma_z + V_{ab}\sigma_x. \end{aligned} \quad (17)$$

The solution to the SRG flow equation is easily found. It is convenient to parametrize the result in terms of  $\theta(s)$  with constant  $\omega$ :

$$\frac{d\theta}{ds} = -2(\epsilon_a - \epsilon_b)\omega \sin \theta(s) \quad (18)$$

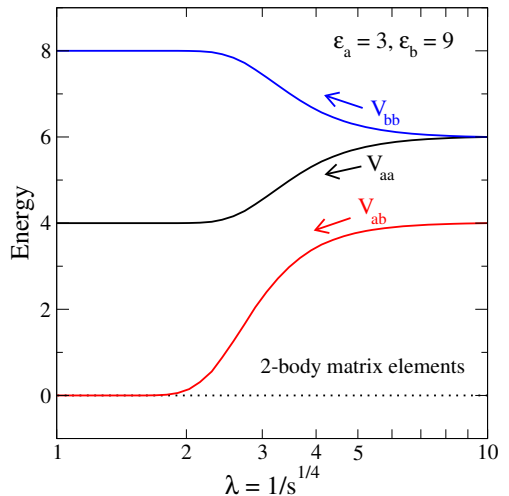


Figure 16: SRG flow for a simple two-state system (see text).

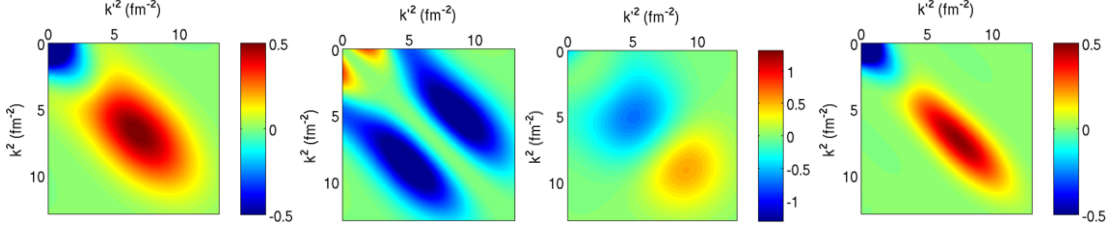


Figure 17: SRG flow in stages. On the far left and far right are potentials in the  ${}^1S_0$  channel evolved to  $\lambda = 2.0 \text{ fm}^{-1}$  and  $\lambda = 1.5 \text{ fm}^{-1}$ , respectively. The middle panels show the first (left) and second (right) terms on the right side of Eq. (23).

where

$$\theta(s) = 2 \tan^{-1} [\tan(\theta(0)/2) e^{-(\epsilon_a - \epsilon_b)\omega s}] , \quad (19)$$

$$\omega \cos \theta = (\epsilon_a - \epsilon_b + V_{aa} - V_{bb})/2 , \quad (20)$$

and

$$\omega \sin \theta = V_{ab} . \quad (21)$$

The resulting flow is plotted for sample energies  $\epsilon_a$  and  $\epsilon_b$  in Fig. 16. We clearly see the off-diagonal matrix element  $V_{ab}$  driven to zero. (Try reproducing this in Mathematica!)

For a nuclear two-body (NN) potential in a partial-wave momentum basis with  $\eta_s = [T, H_s]$ , we project on relative momentum states  $|k\rangle$  using  $1 = \frac{2}{\pi} \int_0^\infty |q\rangle q^2 dq \langle q|$  with  $\hbar^2/M = 1$ . The flow equation reduces to:

$$\frac{dV_s}{ds} = [[T_{\text{rel}}, V_s], H_s] \quad \text{with} \quad T_{\text{rel}}|k\rangle = \epsilon_k|k\rangle \quad (22)$$

and  $\lambda^2 = 1/\sqrt{s}$ .  $T_{\text{rel}}$  is the relative kinetic energy of the nucleons. Then

$$\begin{aligned} \frac{dV_\lambda}{d\lambda}(k, k') &\propto -(\epsilon_k - \epsilon_{k'})^2 V_\lambda(k, k') \\ &+ \sum_q (\epsilon_k + \epsilon_{k'} - 2\epsilon_q) V_\lambda(k, q) V_\lambda(q, k') . \end{aligned} \quad (23)$$

This particular equation is for  $A = 2$ , but the results are generic if one lets  $k$  represent a set of Jacobi momenta. The first term in Eq. (23) drives  $V_\lambda$  toward the diagonal:

$$V_\lambda(k, k') = V_{\lambda=\infty}(k, k') e^{-[(\epsilon_k - \epsilon_{k'})/\lambda^2]^2} + \dots , \quad (24)$$

which can be visualized in Fig. 17. These panels represent a sequence from  $\lambda = 2.0$  to  $\lambda = 1.5$ . The potentials at the beginning and the end are on the outside, while the two middle panels are the first and second term of Eq. (23). For off-diagonal matrix elements, the first term is numerically dominant and each element is driven to zero according to Eq. (24), with further off-diagonal elements changing more rapidly. Note that the width of the diagonal is given roughly by  $\lambda^2$ , in accord with Eq. (24).

A more general proof follows if we use the generator advocated by Wegner, which includes the diagonal part of the Hamiltonian,  $H_d$ . Call the diagonal elements  $H_{ii} = e_i$ , then (with  $\eta_s = [H_d, H_s]$ ),

$$\begin{aligned} \frac{dH_{ij}}{ds} &= \langle i | [[H_d, H_s], H_s] | j \rangle \\ &= \sum_k (e_i + e_j - 2e_k) H_{ik} H_{kj} \\ &= 2 \sum_k (e_i - e_k) |H_{ik}|^2 . \end{aligned} \quad (25)$$

But

$$\begin{aligned} \frac{d}{ds} \sum_i |H_{ii}|^2 &= 2 \sum_i H_{ii} \frac{dH_{ii}}{ds} \\ &= 4 \sum_{i \neq k} e_i (e_i - e_k) |H_{ik}|^2 \\ &= 2 \sum_{i \neq k} (e_i - e_k)^2 |H_{ik}|^2 \geq 0 . \end{aligned} \quad (26)$$

Now use:

$$\text{Tr } H_s^2 = \text{const.} = \sum_{ij} |H_{ij}|^2 = \sum_i |H_{ii}|^2 + \sum_{i \neq j} |H_{ij}|^2 , \quad (27)$$

to obtain

$$\begin{aligned} \frac{d}{ds} \sum_{i \neq j} |H_{ij}|^2 &= -\frac{d}{ds} \sum_i |H_{ii}|^2 \\ &= -2 \sum_{i \neq k} (e_i - e_k)^2 |H_{ik}|^2 \leq 0 . \end{aligned} \quad (28)$$

Thus, in the absence of degeneracies, the off-diagonal matrix elements will decrease (or at least remain unchanged) [1].

This feature of the diagonal generator is desirable, but we also note that for nuclear Hamiltonians in a momentum basis, the diagonal is completely dominated by the kinetic energy, so  $H_d \approx T_{\text{rel}}$  is a very good approximation. Can this break down? Glazek and Perry [21]

showed that it can (see also Wendt et al. [22]). Re-consider the proof of diagonalization, but now with  $G_s = T_{\text{rel}}$ . Now we have  $H_{ii} = e_i$  and  $T_{\text{rel}}|i\rangle = \epsilon_i|i\rangle$ , so that

$$\frac{dH_{ii}}{ds} = 2 \sum_k (\epsilon_i - \epsilon_k) |H_{ik}|^2. \quad (29)$$

So consider

$$\frac{d}{ds} \sum_i |H_{ii}|^2 = 2 \sum_i H_{ii} \frac{dH_{ii}}{ds} = 4 \sum_{i \neq k} e_i (\epsilon_i - \epsilon_k) |H_{ik}|^2, \quad (30)$$

from which we conclude

$$\frac{d}{ds} \sum_{i \neq j} |H_{ij}|^2 = -2 \sum_{i \neq k} (e_i - e_k) (\epsilon_i - \epsilon_k) |H_{ik}|^2. \quad (31)$$

Thus the off-diagonal decrease depends on  $e_i - e_k \approx \epsilon_i - \epsilon_k$ . But there is the possibility of this not being true, e.g., if there are spurious bound states as in large-cutoff EFT [22].

### 3.2. Alternative generators

Other choices of generator are also possible. Recent work by Shirley Li while an undergraduate physics major at Ohio State explored choices designed to accelerate evolution. In particular, one can choose  $G_s$  as

$$G_s = -\frac{\Lambda^2}{1 + T_{\text{rel}}/\Lambda^2} \approx c + T_{\text{rel}} + \dots \quad (32)$$

or

$$G_s = -\Lambda^2 e^{-T_{\text{rel}}/\Lambda^2} \approx c + T_{\text{rel}} + \dots \quad (33)$$

The expansions show that these reduce to the conventional  $T_{\text{rel}}$  for momenta that are small compared to the cutoff parameter  $\Lambda$  (not to be confused with  $\lambda$ ). For  $\Lambda = 2 \text{ fm}^{-1}$ , the low energy part of the potential is still decoupled but there is much less evolution at high energy, which makes it computationally much faster and allows evolution to low  $\lambda$ . See Ref. [23] for details.

The usual approach to  $V_{\text{low } k}$  RG evolution (left diagram in Fig. 8) is based on the Lippmann-Schwinger equation for the half-on-shell T-matrix illustrated in Fig. 18. A cutoff  $\Lambda$  is imposed on the integral in the second term and we demand that matrix elements of  $T$  are invariant with an infinitesimal reduction of  $\Lambda$ . That is, we require  $dT(k, k'; E_k)/d\Lambda = 0$ , which establishes an RG equation for  $V_\Lambda$ . In contrast to the SRG equation, which is second order in the running potential, the  $V_{\text{low } k}$

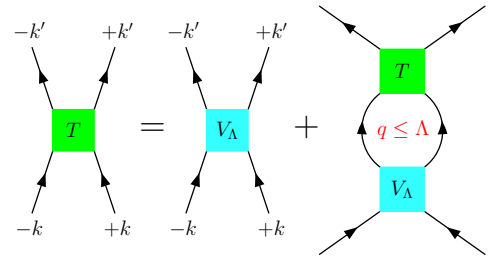


Figure 18: Schematic version of the Lippmann-Schwinger equation for the T-matrix, with cutoff  $\Lambda$  on the intermediate states. The  $V_{\text{low } k}$  potential  $V_\Lambda$  is determined by requiring half-on-shell matrix elements of this equation to be invariant under changes in  $\Lambda$  [7, 2].

RG equation has the T-matrix on the right side. Thus

$$\begin{aligned} T(k', k; k^2) &= V_{\text{NN}}(k', k) \\ &+ \frac{2}{\pi} \mathcal{P} \int_0^{\Lambda} \frac{V_{\text{NN}}(k', p) T(p, k; k^2)}{k^2 - p^2} p^2 dp \\ &= V_{\text{low } k}^\Lambda(k', k) \\ &+ \frac{2}{\pi} \mathcal{P} \int_0^\Lambda \frac{V_{\text{low } k}^\Lambda(k', p) T(p, k; k^2)}{k^2 - p^2} p^2 dp \end{aligned} \quad (34)$$

for all  $k, k' < \Lambda$ . (Note: we are using standing-wave boundary conditions for numerical reasons; this is often called the K-matrix.) From  $dT/d\Lambda = 0$ , we get the  $V_{\text{low } k}$  RG equation:

$$\frac{d}{d\Lambda} V_{\text{low } k}^\Lambda(k', k) = \frac{2}{\pi} \frac{V_{\text{low } k}^\Lambda(k', \Lambda) T^\Lambda(\Lambda, k; \Lambda^2)}{1 - (k/\Lambda)^2}. \quad (35)$$

Note that the full T matrix appears on the right side, in contrast to the partial-wave SRG flow equation (with  $G_s = T_{\text{rel}}$ ),

$$\begin{aligned} \frac{d}{d\lambda} V_\lambda(k, k') &\propto -(\epsilon_k - \epsilon_{k'})^2 V_\lambda(k, k') \\ &+ \sum_q (\epsilon_k + \epsilon_{k'} - 2\epsilon_q) V_\lambda(k, q) V_\lambda(q, k'), \end{aligned} \quad (36)$$

which is only second-order in the potential. We can also define smooth regulators for  $V_{\text{low } k}$  as in Ref. [24].

The evolution of NN potentials using the  $V_{\text{low } k}$  method is illustrated for a sharp and smooth regulator in Fig. 19. Comparing the  $V_{\text{low } k}$  flow in these figures to the SRG flow in Fig. 9, we see the same decoupling of low and high momentum. Other non-RG unitary transformations (which perform the transformation all at once, rather than in steps) also decouple; an example is the UCOM method [25], which has close connections to the SRG (see Refs. [26, 27]).

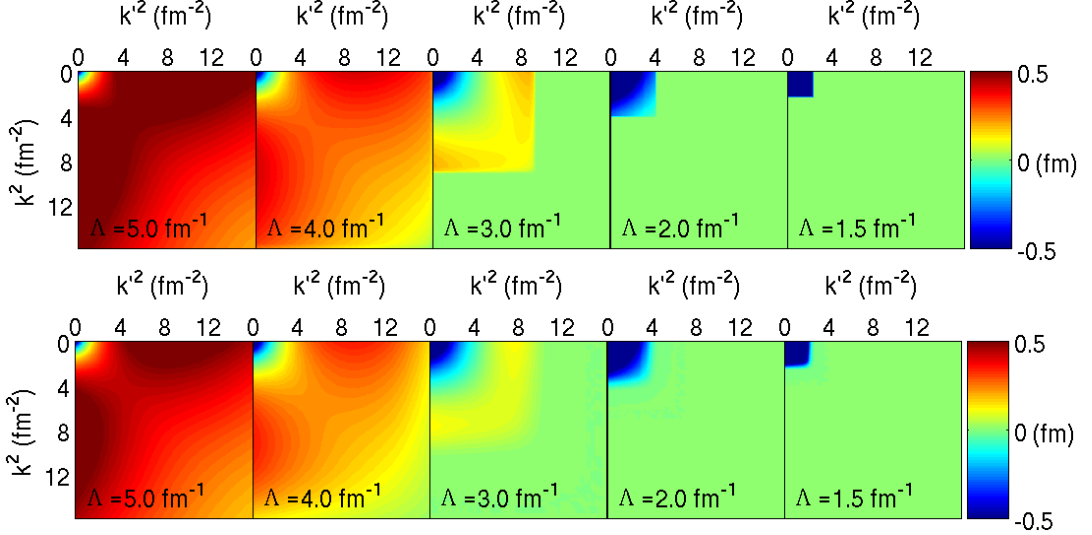


Figure 19:  $V_{\text{low } k}$  flow of AV18 in the  ${}^3\text{S}_1$  channel for a sharp (top) and smooth (bottom) regulator [24].

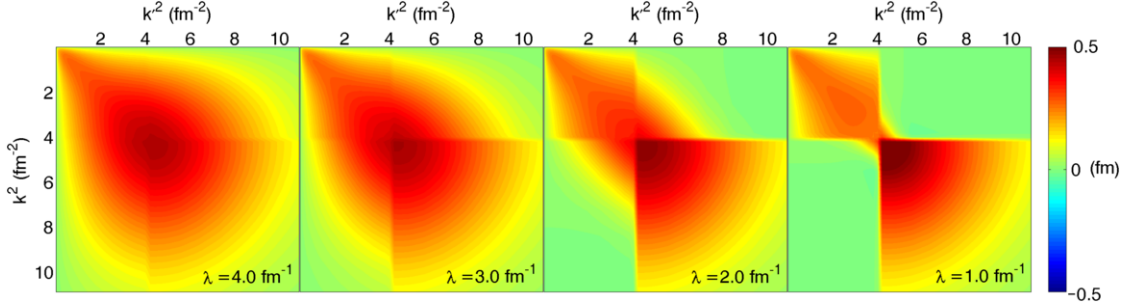


Figure 20: SRG sharp block-diagonal flow of AV18 in the  ${}^1\text{P}_1$  channel at  $\lambda = 4, 3, 2$ , and  $1 \text{ fm}^{-1}$  [28]. The initial  $\text{N}^3\text{LO}$  potential is from Ref. [29] and  $\Lambda = 2 \text{ fm}^{-1}$ . The axes are in units of  $k^2$  from 0 to  $11 \text{ fm}^{-2}$  and the color scale is from  $-0.5$  to  $+0.5 \text{ fm}$ .

It is also possible to choose a generator that reproduces the block diagonal (as opposed to band diagonal) form of the  $V_{\text{low } k}$  RG shown schematically in Fig. 8, except that the transformation will be unitary. In particular, we can use

$$\frac{dH_s}{ds} = [[G_s, H_s], H_s] \quad (37)$$

with

$$G_s = \begin{pmatrix} PH_s P & 0 \\ 0 & QH_s Q \end{pmatrix}, \quad (38)$$

where projection operators  $P$  and  $Q = 1 - P$  are simply step functions at a given  $\Lambda$  in partial-wave momentum representation. An example of the subsequent flow is shown in Fig. 20 for the  ${}^1\text{P}_1$  channel [28]. To get the fully block-diagonal form, one would have to evolve to  $\lambda = \infty$ . But in practice, going to  $\lambda = 1 \text{ fm}^{-1}$  is sufficient for essentially complete decoupling at  $\Lambda = 2 \text{ fm}^{-1}$ .

The proof of block diagonalization (see Gubankova et al. [30, 31]) goes as follows. The generator  $\eta_s = [G_s, H_s]$  is non-zero only where  $G_s$  is zero, which means in the off-diagonal blocks. This will then evolve the potential in this same pattern (this is generically true, if one desires a different pattern [28]). A measure of off-diagonal coupling of  $H_s$  is

$$\text{Tr}[(QH_s P)^\dagger (QH_s P)] = \text{Tr}[PH_s QH_s P] \geq 0. \quad (39)$$

Now we can calculate the derivative of this expression by applying the SRG equation (37):

$$\begin{aligned} \frac{d}{ds} \text{Tr}[PH_s QH_s P] &= \\ &\text{Tr}[P\eta_s Q(QH_s QH_s P - QH_s PH_s P)] \\ &+ \text{Tr}[(PH_s PH_s Q - PH_s QH_s Q)Q\eta_s P] \\ &= -2 \text{Tr}[(Q\eta_s P)^\dagger (Q\eta_s P)] \leq 0. \quad (40) \end{aligned}$$

Thus the off-diagonal  $QH_sP$  block will decrease as  $s$  increases.

The low-momentum block of this SRG is found to be remarkably similar to the corresponding  $V_{\text{low } k}$  RG potential. Examples are shown in Figs. 21 and 22. However, *proving* that these different RG approaches should yield the same potential remains an open problem.

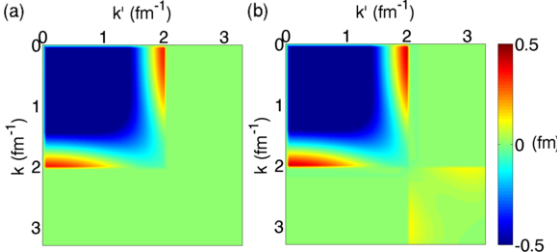


Figure 21: Comparison of momentum-space (a)  $V_{\text{low } k}$  and (b) SRG block-diagonal  $^3S_1$  potentials with  $\Lambda = 2 \text{ fm}^{-1}$  [28].

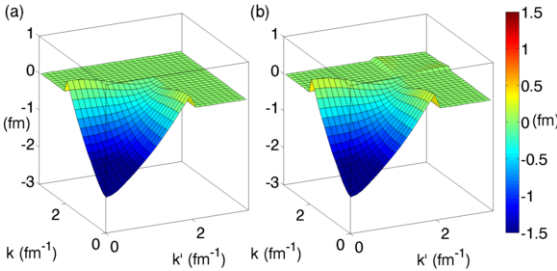


Figure 22: Same as Fig. 21, only a surface plot.

### 3.3. Many-body forces

In Fig. 23, the convergence of the triton ground-state energy with harmonic oscillator basis size ( $N_{\text{max}}\hbar\omega$  excitations) is shown for two chiral EFT NN potentials and for the corresponding SRG-evolved potentials at  $\lambda$ 's from  $4 \text{ fm}^{-1}$  to  $1 \text{ fm}^{-1}$ . In accord with our previous discussion, we see increasingly rapid convergence as  $\lambda$  decreases. (Note that there is softening already at  $\lambda = 3 \text{ fm}^{-1}$  for the N<sup>3</sup>LO EFT with  $\Lambda = 600 \text{ MeV}$ , which corresponds to  $3 \text{ fm}^{-1}$ . The moral is that it is not sufficient to simply compare the cutoff numerically to the decoupling scale  $\lambda$ .) However, we also see that the converged (or extrapolated) binding energies are different for each  $\lambda$ ! How could this be, if the SRG is supposed to generate unitary transformations?

There are further signs of trouble, such as nuclear matter failing to saturate after the two-body potential is softened by RG evolution. Let's review the facts about uniform nuclear matter. Figure 24 shows the binding

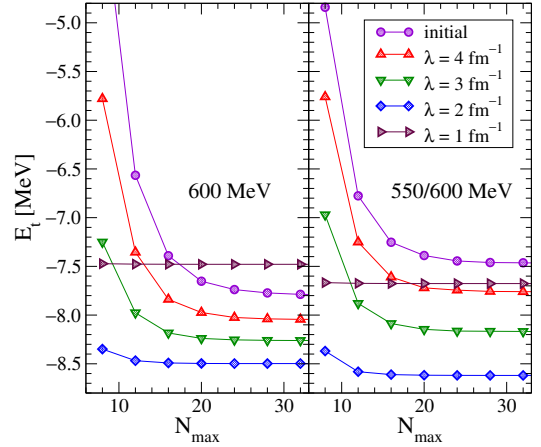


Figure 23: Convergence of three-body energies for two potentials and several sets of  $\lambda$ 's.

energy per particle for pure neutron matter ( $Z = 0$ ) and symmetric nuclear matter ( $N = Z = A/2$ ) from calculations adjusted to be consistent with extrapolations from nuclei. Neutron matter has positive pressure, while symmetric nuclear matter *saturates*; that is, there is a minimum at a density of about  $0.16 \text{ fm}^3$  with a binding energy of about  $-16 \text{ MeV/A}$ . Reproducing this minimum with microscopic interactions fit only to few-body data is one of the holy grails of nuclear structure theory. But if we evolve an NN potential with either the  $V_{\text{low } k}$  RG or the SRG, we find that nuclear matter does not converge. This is shown for  $V_{\text{low } k}$  by the “NN only” curves in Fig. 25 and similar behavior is found for SRG.

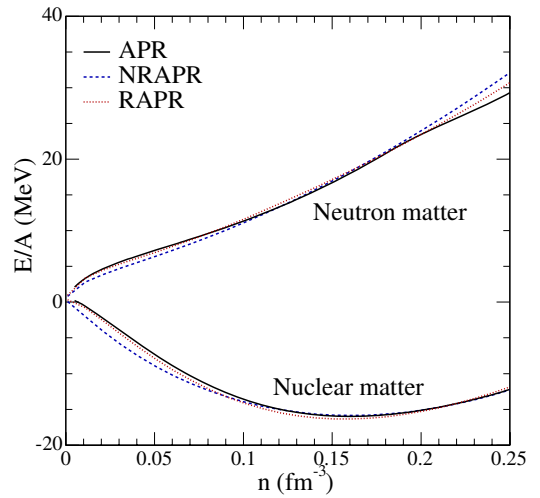


Figure 24: Binding energies of nuclear and neutron matter from Akmal et al. for several equations of state [32].

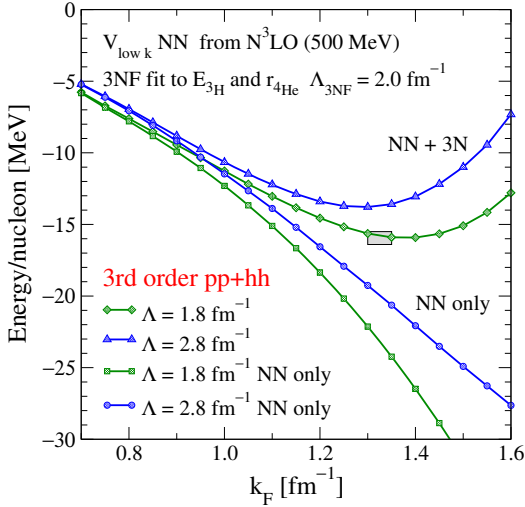


Figure 25: Nuclear matter at third order in perturbation theory in the particle-particle channel (this appears sufficient for convergence) using a  $V_{\text{low } k}$  RG-evolved potential [33]. The “NN only” curves include no three-body interactions while the “NN + 3N” curves include a 3NF fit to the triton binding energy and the alpha particle radius.

The failure of softened low-momentum potentials to reproduce nuclear matter saturation should sound familiar to anyone who knows the long history of low-energy nuclear theory. There were active attempts to transform away hard cores and soften the tensor interaction in the late sixties and early seventies. But the requiem for soft potentials was given by Bethe in 1971 [34]: “Very soft potentials must be excluded because they do not give saturation; they give too much binding and too high density. In particular, a substantial tensor force is required.” The next thirty-five years were spent struggling to solve accurately with such “hard” potentials. But the story is not complete: the three-nucleon forces (3NF) were not properly accounted for!

Three-body forces between protons and neutrons have a classical analog in tidal forces: the gravitational force on the Earth is not just the pairwise sum of Earth-Moon and Earth-Sun forces. Quantum mechanically, an analog is with the three-body force between atoms and molecules, which is called the Axilrod-Teller term and dates from 1943 [35]. The origin is from triple-dipole mutual polarization. It is a third-order perturbation correction, so the weakness of the fine structure constant means that these forces are usually negligible in metals and semiconductors. However, in solids bound by van der Waals potentials it can be significant; for example, it is ten percent of the binding energy in solid xenon [36]. This is the same relative size as needed in the triton.

In general, three-body forces arise from eliminating

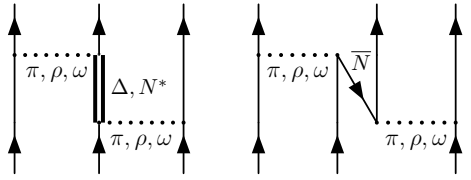


Figure 26: Sources of internucleon three-body forces. On the left, the intermediate state includes an excitation of the nucleon ( $\Delta$  or  $N^*$ ). On the right, the intermediate state includes a virtual anti-nucleon ( $\bar{N}$ ). When these degrees of freedom are integrated out, the resulting nucleons-only vertex is a 3NF.

degrees of freedom. In the nuclear case, this can mean eliminating excited states of the nucleon ( $N^*$  or  $\Delta$ ) or from relativistic effects; see Fig. 26 for diagrammatic representations. If the intermediate states are not included in the low-energy degrees of freedom, we have irreducible vertices with three nucleons in and three nucleons out. But 3NF’s also result from the decoupling of high-momentum intermediate states, whether they are eliminated explicitly by a cutoff (as with the  $V_{\text{low } k}$  RG) or the degree of coupling modified (as with the SRG). Omitting three-body forces leads to model dependence: observables will depend on the decoupling scale, whether it is the  $V_{\text{low } k}$   $\Lambda$  or the SRG  $\lambda$ . This dependence also becomes a tool, because it is a diagnostic for errors (more on this later). To eliminate this dependence, the 3NF at different  $\Lambda$  or  $\lambda$  must be either fit or evolved.

It is easy to see that RG flow equations lead to many-body operators. Consider the SRG operator flow equation written with second-quantized  $a$ ’s and  $a^\dagger$ ’s:

$$\begin{aligned} \frac{dV_s}{ds} &= \left[ \left[ \sum_{G_s} \underbrace{a^\dagger a}_{\text{2-body}}, \sum_{G_s} \underbrace{a^\dagger a^\dagger aa}_{\text{2-body}} \right], \sum_{G_s} \underbrace{a^\dagger a^\dagger aa}_{\text{2-body}} \right] \\ &= \dots + \underbrace{\sum_{\text{3-body}} a^\dagger a^\dagger a^\dagger aaa}_{\text{3-body!}} + \dots \end{aligned} \quad (41)$$

where the second equality reflects that even if the initial Hamiltonian is two-body, the commutators give rise to three-body terms. (For future reference, recall that the creation and destruction operators are always defined with respect to a single-particle basis and a reference state, which in this case is the vacuum.)

As the evolution continues, there inevitably will be  $A$ -body forces (and operators) generated. Is this a problem? Not if these “induced” many-body forces are the same size as those that naturally occur. Indeed, nuclear three-body forces are already needed in almost all potentials in common use to get even the triton binding

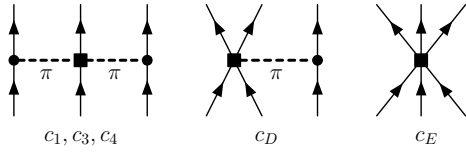


Figure 27: Leading three-body forces from chiral EFT. These contributions represent three different ranges: long-range 2-pion exchange, short-range contact with one-pion exchange, and pure contact interaction.

energy correct. In fact, low-energy effective theory tell us generalized diagrams such as those in Fig. 26 with four or more legs imply that there are  $A$ -body forces (and operators) initially!

However, there is a natural hierarchy predicted from chiral EFT, whose leading contributions are given in Fig. 27 (we'll return to this in Section 4.1 and supply additional details). If we stop the flow equations before induced  $A$ -body forces are unnaturally large or if we can tailor the SRG  $G_s$  to suppress their growth, we will be ok. (Another option is to choose a non-vacuum reference state, which is what is done with in-medium SRG, to be discussed later.) Note that analytic bounds on  $A$ -body growth have not been derived, so we need to explicitly monitor the contribution in different systems. But the bottom line that makes the SRG attractive as a method to soften nuclear Hamiltonians is that it is a tractable method to evolve many-body operators.

To include the 3NF using SRG with normal-ordering in the vacuum, we start with the SRG flow equation  $dH_s/ds = [[G_s, H_s], H_s]$  (e.g., with  $G_s = T_{\text{rel}}$ ). The right side is evaluated without solving bound-state or scattering equations, unlike the situation with  $V_{\text{low } k}$ , so the SRG can be applied directly in the three-particle space. The key observation is that for normal-ordering in the vacuum,  $A$ -body operators are completely fixed in the  $A$ -particle subspace. Thus we can first solve for the evolution of the two-body potential in the  $A = 2$  space, with no mention of the 3NF (either initial or induced), and then use this NN potential in the equations applied to  $A = 3$ .

What about spectator nucleons? There is a decoupling of the 3NF part. We can see this from the first-quantized version of the SRG flow equation,

$$\begin{aligned} \frac{dV_s}{ds} &= \frac{dV_{12}}{ds} + \frac{dV_{13}}{ds} + \frac{dV_{23}}{ds} + \frac{dV_{123}}{ds} \\ &= [[T_{\text{rel}}, V_s], H_s], \end{aligned} \quad (42)$$

where we isolate the contributions from each pair and the 3NF. Using each SRG equation for the two-body derivatives, we can cancel them against terms on the

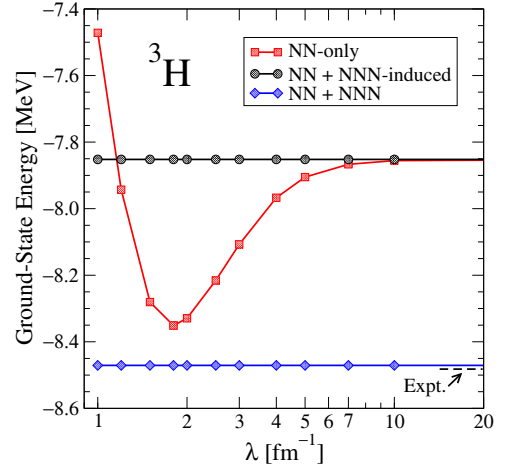


Figure 28: Triton binding energy during SRG evolution. The three curves are for an initial potential with only NN components where the induced 3NF is not kept (“NN-only”), for the same initial NN potential but keeping the induced 3NF (“NN + NNN-induced”), and with an initial NNN included as well (“NN + NNN”).

right side. The result is [12]:

$$\begin{aligned} \frac{dV_{123}}{ds} &= [[T_{12}, V_{12}], (T_3 + V_{13} + V_{23} + V_{123})] \\ &\quad + \{123 \rightarrow 132\} + \{123 \rightarrow 231\} \\ &\quad + [[T_{\text{rel}}, V_{123}], H_s]. \end{aligned} \quad (43)$$

The key is that there are no “multi-valued” two-body interactions remaining (i.e., dependence on the excitation energy of unlinked spectators); all the terms are connected. An implementation of these equations in a momentum basis would be very useful and has very recently been achieved by Hebeler [37]. But an alternative approach has also succeeded: a direct solution in a discrete basis [38, 16, 17].

The idea is that the SRG flow equation is an operator equation, and thus we can choose to evolve in any basis. If one chooses a discrete basis, than a separate evolution of the three-body part is not needed. This was first done for nuclei by Jurgenson and collaborators in 2009 using an anti-symmetrized Jacobi harmonic oscillator (HO) basis [16]. The technology for working with such a basis had already been well established for applications to the no-core shell model (NCSM) [39]. This approach leads to SRG-evolved matrix elements of the potential directly in the HO basis, which is just what is needed for many-body applications such as NCFC or coupled cluster.

In Fig. 28, the comparison of two-body-only to full two-plus-three-body evolution is shown for the triton ( ${}^3\text{H}$ ). The NN-only curve uses the evolved two-body

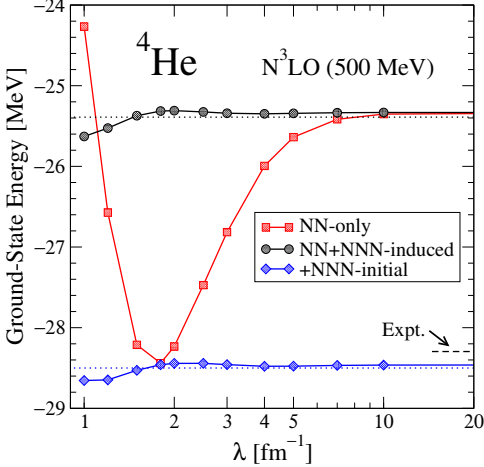


Figure 29: Alpha particle binding energy during SRG evolution. The curves correspond to those in Fig. 28.

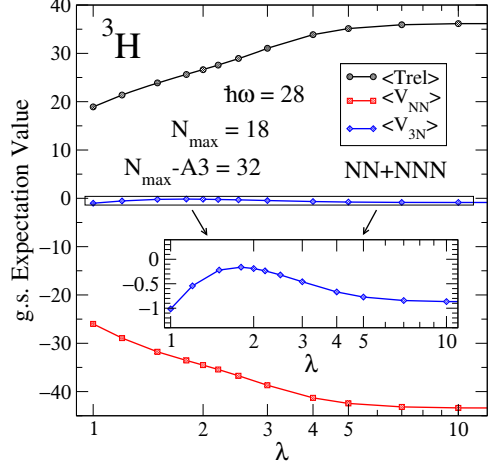


Figure 31: Contributions to the triton binding energy during SRG evolution. Plotted are the expectation values of the kinetic energy, the two-body potential, and the three-body potential [17].

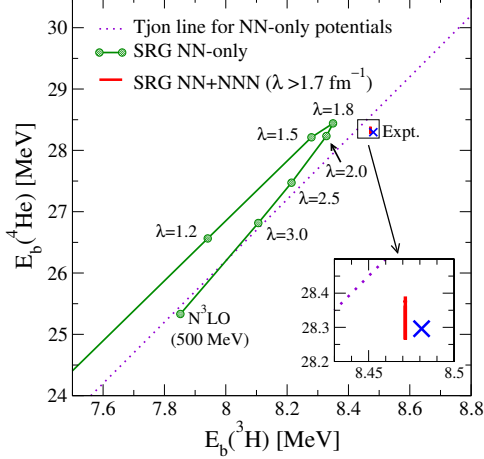


Figure 30: Correlation plot of the binding energies of the alpha particle and the triton. The dotted line connects (approximately) the locus of points found for phenomenological potentials, and is known as the Tjon line [40].

potential. The change in energy with  $\lambda$  reflects the violation of unitarity by omission of the induced three-body force. When this induced 3NF is included (“NN + NNN-induced”), the energy is independent of  $\lambda$  for  $A = 3$ . If we now turn to the alpha particle ( ${}^4\text{He}$ ) in Fig. 29, we see similar behavior, except now the inclusion of the induced 3NF does not lead to a completely flat curve at the lowest  $\lambda$  values. If there is sufficient convergence, this is a signal of missing induced 4NF.

In both cases, it is evident that starting with an initial NN-only interaction (in this case, an  $N^3\text{LO}(500 \text{ MeV})$

interaction [29]), does not reproduce experiment. The third line in each plot of Figs. 28 and 29 shows that an initial 3NF (labeled NNN) contribution leads to a good reproduction of experiment. The triton energy is part of the fit of this initial force, but the alpha particle energy is a prediction. Note that the magnitude of the NN-only variation is comparable to the initial 3NF needed. This is an example of the natural size of the 3NF being manifested by the running of the potential (which is, in effect, the beta function).

The nature of the evolution is illustrated in Fig. 30, which is a correlation plot of the binding energies in each nucleus. The dotted line is known as the Tjon line for NN-only phenomenological potentials. It was found that different potentials that fit NN scattering data gave different binding energies, but that they clustered around this line. With the SRG evolution starting with just an NN potential, the path follows the line, passing fairly close to the experimental point. With an initial NNN force and keeping the induced 3-body part, the trajectory is greatly reduced (see inset), at least until  $\lambda$  is small.

Figures 31 and 32 show individual contributions to the energy in the form of ground-state matrix elements of the kinetic energy, two-body, three-body, and (implied) four-body potentials. The hierarchy of contributions is quite clear but the graphs also manifest the strong cancellations between the NN and kinetic energy contributions. These cancellations magnify the impact of higher-body forces. Even so, it appears that a truncation including the NNN but omitting higher-body forces

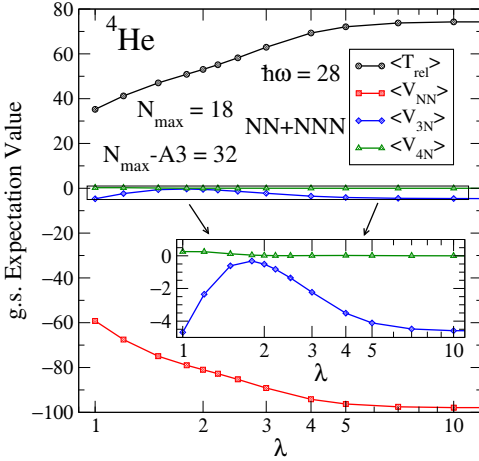


Figure 32: Contributions to the alpha particle binding energy during SRG evolution. Plotted are the expectation values of the kinetic energy, the two-body potential, the three-body potential, and the four-body potential [17].

is workable, particularly with  $\lambda > 1.5 \text{ fm}^{-1}$ . But what about the  $A$  dependence of the 4NF (and beyond)?

This  $A$  dependence is the topic of current research. In Fig. 33, results for  ${}^6\text{Li}$  are shown [17]. Assessing these results is made difficult because of insufficient convergence of comparison calculations (the shaded areas) and of calculations at the large  $\lambda$  values. Note, however, that the variations are with the 1 MeV level; nevertheless we expect to do better.

Roth and collaborators have since used importance truncated NCSM (IT-NCSM) to extend these calculations to much higher  $N_{\max}$  and all the way to  ${}^{16}\text{O}$  [19]. They find that the SRG with initial NN-only but including the induced NNN shows only small running with  $\lambda$ . On the other hand, with increasing  $A$  they find significant deviations. This has been traced to the influence of the initial long-range NNN interaction. If they lower the cutoff of this part of the interaction, then approximate SRG unitarity is restored and with coupled-cluster methods they find reasonable results even for medium-size nuclei (although not yet with fully consistent Hamiltonians) [41].

### 3.4. Summary points

Renormalization group flow equations dramatically reduce correlation in many-body wave functions, leading to faster convergence of many-body calculations. Flow equations (SRG) achieve this lower resolution by decoupling via a series of unitary transformations, which leave observables invariant (if no approximations are made) but alter the physics interpretation. Few-body

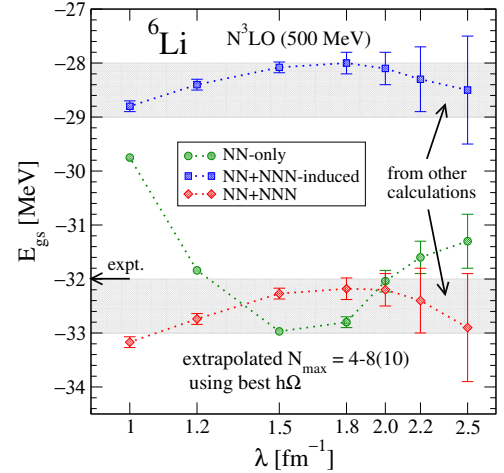


Figure 33: SRG running of the  ${}^6\text{Li}$  ground-state energy. The error bars are estimates of the errors from extrapolating the results to  $N_{\max} = \infty$ . The gray shaded region shows the uncertainty from NSCM calculations using a Lee-Suzuki effective interaction [17].

forces are inevitable, but the flow-equation approach allows the evolution of vacuum interactions.

## 4. Features of SRG applied to nuclear problems

### 4.1. Chiral EFT, many-body forces, and the SRG

Before continuing with the SRG for nuclear systems, let's say a bit more about chiral effective field theory (EFT). In the SRG flow equations, the input interaction is merely an initial condition; the equations are the same whether we start with an EFT potential or a more phenomenological potential such as Argonne  $v_{18}$ . However, increasingly nuclear theorists are moving toward using EFT interactions because they promise a more systematic construction of many-body forces and consistent operators.

There are three fundamental ingredients of an effective field theory (e.g., see Ref. [42]). The first is to use the most general lagrangian with low-energy degrees of freedom consistent with the global and local symmetries of the underlying theory. For nuclei, the underlying theory is quantum chromodynamics (QCD). We can identify a hierarchy of nuclear QCD scales:

- $M_{\text{QCD}} \sim 1 \text{ GeV}$  [ $M_{\text{hadrons}}, 4\pi f_\pi$ ]
- $M_{\text{nuc}} \sim 100 \text{ MeV}$  [ $k_F, f_\pi, m_\pi, \delta_{\Delta N}$ ]
- $M_{\text{nuc}}^2/M_{\text{QCD}} \sim 10 \text{ MeV}$  [nuclear binding energy per nucleon]

For all but the lightest nuclei, the EFT of choice at present draws a line between the first two levels to define the high-energy and low-energy scales. This is the chiral EFT, with degrees of freedom consisting of the nucleon (proton and neutron) and the pion [43]. In the near future, the  $\Delta$  resonance will be included as well because of the small mass difference with the nucleon,  $\delta_{\Delta N}$ . Besides the usual space-time symmetries, terms in the chiral EFT lagrangian are constrained by the requirements of spontaneously broken (as well as explicitly broken) chiral symmetry [43].

The other two ingredients are the declaration of a regularization and renormalization scheme, and the identification of a well-defined power counting based on well-defined expansion parameters. The separation of scales provides the expansion parameter as ratios of  $Q/M_{\text{QCD}}$ , where  $Q$  is one of the quantities lumped together above as  $M_{\text{nuc}}$ . The chiral EFT potentials used here are derived using a momentum cutoff and what is called “Weinberg counting”, in which the counting is done at the level of an irreducible potential that is summed non-perturbatively with the Lippmann-Schwinger equation. This scheme has been criticized because it does not allow systematic renormalization (meaning, in this context, the removal of cutoff dependence at each order), which limits the range of cutoffs used. This in turn hinders the validation of the EFT, because the sensitivity to the cutoff is used as a measure of uncertainties. See Ref. [43] for a thorough overview of chiral EFT for nuclei and the status of the power counting and renormalization controversies.

With any scheme, however, the power counting implies a hierarchy of many-body contributions. Weinberg counting associates a power  $v$  of  $Q/M_{\text{QCD}}$  with diagrams for the potential, where

$$v = -4 + 2N + 2L + \sum_i (d_i + n_i - 2). \quad (44)$$

The definitions and details of its implementation can be found in Ref. [43]. For our purposes, the relevant term is “ $2N$ ”, which says that adding a nucleon to go from an  $A$ -body potential to an  $A + 1$ -body potential generally suppresses the contribution by  $Q^2/M_{\text{QCD}}$ . In the theory without  $\Delta$ 's, the suppression of the leading 3NF compared to the leading NN interaction is actually  $(Q/M_{\text{QCD}})^3$ , and a four-body force first appears at order  $(Q/M_{\text{QCD}})^4$  [43]. It is this hierarchy that we want to preserve as we run our SRG flow equations.

As noted, the flow equation technology discussed here does not rely on a particular implementation of chiral EFT, except that the SRG is inherently non-perturbative. This apparently excludes alternative renor-

malization and power counting schemes that require a perturbative treatment beyond leading order [44, 45, 46]. The current belief is that the two approaches should give comparable results as long as the EFT cutoff is taken to be of order  $M_{\text{QCD}}$ , but the issue is far from settled [43].

Another consideration is whether one could bypass the SRG by simply applying chiral EFT with a lower cutoff. Indeed, there exists low-cutoff implementations on the market that display similar characteristics to low-momentum RG-evolved interactions. However, the lower cutoff also means the effective expansion parameter is smaller, and therefore the truncation error is reduced. With the RG, one preserves the truncation error from the cutoff of order  $M_{\text{QCD}}$ . An additional advantage of the RG is the controlled variation of the decoupling scale, which provides a tool for assessing errors from the Hamiltonian truncation and many-body approximations. But this is also not a settled issue and further study would be welcome.

#### 4.2. More perturbative nuclear systems flow equations

Earlier we mentioned the role of RG in high-energy physics in improving perturbation theory. Much of low-energy nuclear physics is intrinsically non-perturbative because of large scattering lengths and bound states, so how do we quantify “perturbativeness”? We study the convergence of the Born series for scattering to see how this can be done.

Consider whether the Born series for the T-matrix operator at a given (complex)  $z$ ,

$$T(z) = V + V \frac{1}{z - H_0} V + V \frac{1}{z - H_0} V \frac{1}{z - H_0} V + \dots \quad (45)$$

converges. This is something like a geometric series, for which we know clearly the convergence criterion:  $1 + w + w^2 + \dots$  diverges if  $|w| \geq 1$ . We get a clue for how to use this if we consider a bound state  $|b\rangle$  and the special value  $z = E_b$ , which is the bound-state energy. Then we can rearrange the Schrödinger equation

$$(H_0 + V)|b\rangle = E_b|b\rangle \quad (46)$$

to the form

$$\frac{1}{E_b - H_0} V|b\rangle = |b\rangle \quad (47)$$

and look at  $T(E_b)|b\rangle$ . Using Eq. (47) repeatedly, the divergence is manifest, i.e., we get  $V(1 + 1 + 1 + \dots)|b\rangle$ .

Now we see that we can generalize Eq. (47) for fixed  $E$  by looking for eigenstates of  $(E - H_0)^{-1}V$  with eigenvalue  $\eta_v(E)$ ,

$$\frac{1}{E - H_0} V|\Gamma_v\rangle = \eta_v(E)|\Gamma_v\rangle. \quad (48)$$

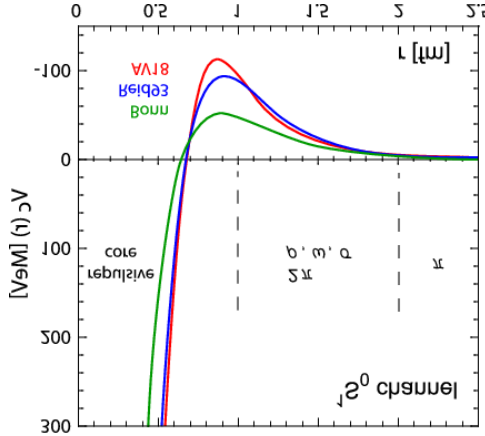


Figure 34: The potentials of Fig. 3 inverted as part of the Weinberg eigenvalue analysis (see text).

Then with  $T$  applied to these eigenstates, there is manifestly a divergence for  $|\eta_\nu(E)| \geq 1$ :

$$T(E)|\Gamma_\nu\rangle = V|\Gamma_\nu\rangle(1 + \eta_\nu + \eta_\nu^2 + \dots). \quad (49)$$

So we characterize the perturbativeness of a potential at energy  $E$  by the  $\eta_\nu(E)$  with the largest magnitude, which dictates convergence of the  $T$  matrix. This analysis follows work in the early 1960's by Weinberg [48], so we call  $\eta_\nu$  a "Weinberg eigenvalue", although others have made similar treatments of the convergence of the Lippmann-Schwinger series.

If we compare Eq. (48) to Eq. (47), we can express the convergence criterion for  $E < 0$  as saying that  $T(E)$

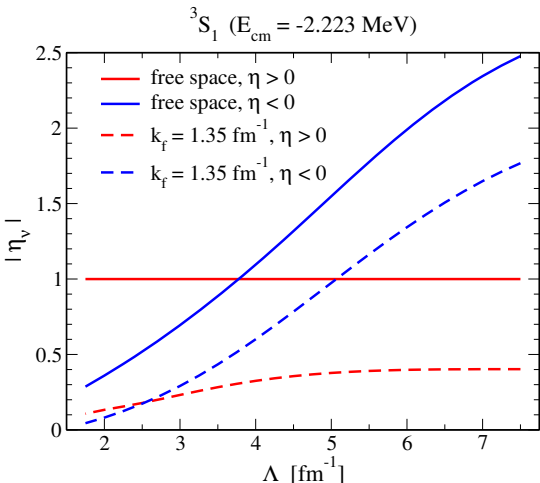


Figure 35:  $V_{\text{low } k}$  RG evolution of the largest positive and negative Weinberg eigenvalue at fixed energy (corresponding to the deuteron binding energy) for AV18 in the  $^3S_1$  channel [47].

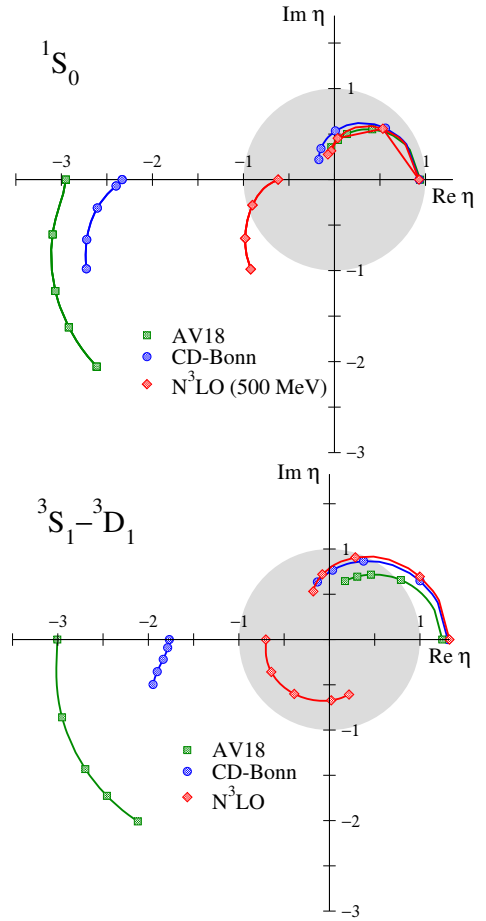


Figure 36: Trajectories of Weinberg eigenvalues in the complex plane for several realistic NN potentials in two channels. The symbols go from 0 MeV on the axis to 25, 66, 100, and 150 MeV [47].

diverges if there exists a bound state at  $E$  for  $V/\eta_\nu$  with  $|\eta_\nu| \geq 1$ . Or, in other words, what is the largest  $\eta_\nu$  for which  $V/\eta_\nu$  supports a bound state at  $E$ ? We have convergence only for  $\eta_\nu < 1$ . This means we'll have two types of eigenvalues, because  $\eta_\nu$  could be negative ("repulsive") as well as positive ("attractive"). The negative eigenvalue corresponds to looking for bound states with a scaled "flipped" potential, as in Fig. 34. We see that the repulsive core becomes a deep attractive well, implying that we will have a large negative eigenvalue in these cases. But then we expect that RG evolution to a softened form, which eliminates the core, should result in decreased eigenvalues.

These expectations hold in practice, as illustrated in Fig. 35, which shows the evolution of the largest positive and negative Weinberg eigenvalues as a function of the  $V_{\text{low } k}$  cutoff  $\Lambda$ . (Very similar behavior is observed for the SRG with  $\lambda$  replacing  $\Lambda$ .) In free space, the largest attractive eigenvalue is unity at all  $\Lambda$ 's, corre-

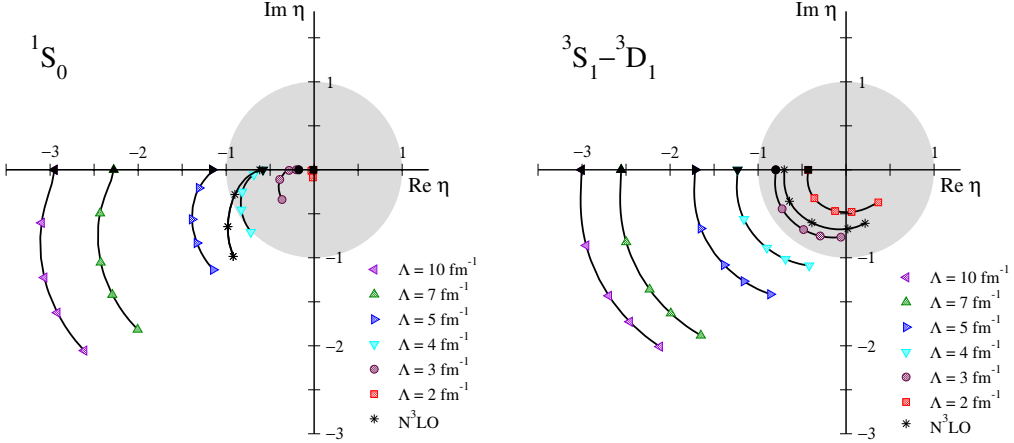


Figure 37: Trajectories of Weinberg eigenvalues in the complex plane for the AV18 NN potential in two channels at various states in a  $V_{\text{low}_k}$  RG evolution (labeled by  $\Lambda$ ). The symbols go from 0 MeV on the axis to 25, 66, 100, and 150 MeV [47].

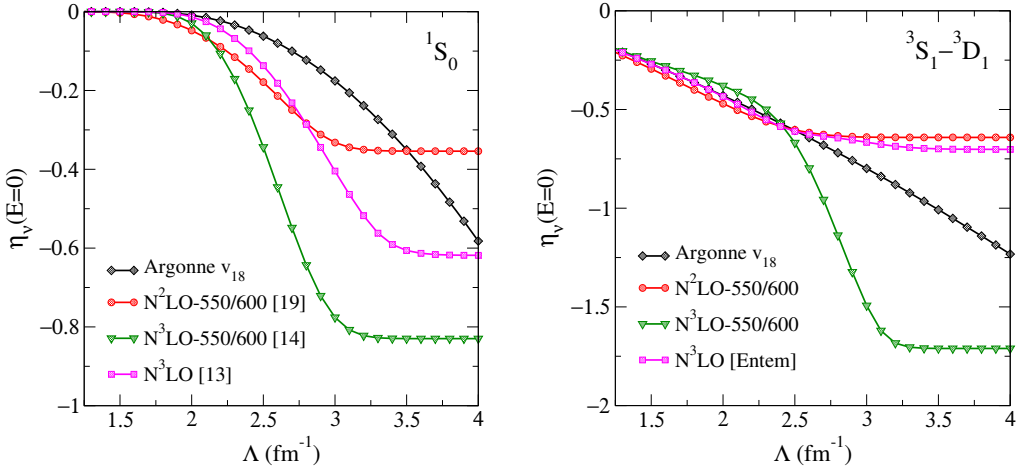


Figure 38: Repulsive (negative) Weinberg eigenvalues at  $E = 0$  for several  $N^3LO$  chiral EFT potentials as a function of  $V_{\text{low}_k} \Lambda$  [47].

sponding to the deuteron bound state. But the negative eigenvalue starts very large (because of the repulsive core) and drops dramatically as the potential is evolved, ending up well less than unity, indicating it is perturbative (but the positive eigenvalue still makes this channel nonperturbative). The situation is even more dramatic in the medium. The other curves in the figure show the result from considering the T matrix in the nuclear medium, where Pauli blocking effects are included in the intermediate states. We see a further reduction of the negative eigenvalue and now the positive eigenvalue is perturbative as well: the deuteron has dissolved!

Starting from negative energies, we can follow the evolution of the largest eigenvalue into the complex plane as we increase  $E$  to positive values. Figures 36 and 37 show paths in the complex plane for Weinberg

eigenvalues, with the symbols indicating energies of 0, 25, 66, 100, and 150 MeV. The shaded region is the unit circle; the potential is perturbative for energies where both eigenvalues lie inside. The softening effect of the RG evolution is manifest in Fig. 37 and the eigenvalues provide a quantitative measure of the perturbativeness. It's also clear from Fig. 36 that at least the particular chiral potential used there is already quite soft. However, Fig. 38 shows that significant *additional* softening is possible with RG evolution. In all of these plots, the differences between the  $^1S_0$  channel and the  $^3S_1 - ^3D_0$  coupled channel stem from the latter having an additional source of nonperturbative behavior: the short-range tensor force.

The increasing “perturbativeness” at finite density is documented again in Fig. 39. At typical nuclear densi-

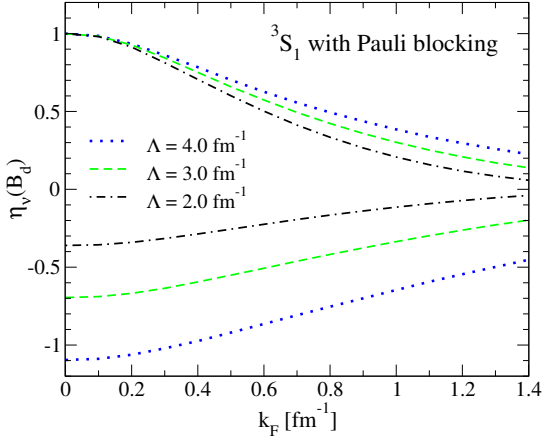


Figure 39: Dependence of the largest Weinberg eigenvalues on density for several evolved  $V_{\text{low } k}$  potentials [47].

ties with  $1 \text{ fm}^{-1} \leq k_F \leq 1.3 \text{ fm}^{-1}$ , both positive and negative eigenvalues are small at the lowest  $\Lambda$ 's. This implies that nuclear matter may actually be perturbative! (Note that at the Fermi surface, pairing as a nonperturbative phenomenon is revealed by  $|\eta_v| > 1$  [49].) We can understand how this happens from Fig. 40, which shows the phase space available to two nucleons that scatter in the medium. Pauli blocking means they must go outside the two Fermi spheres, but the volume is increasingly restricted with decreasing  $\Lambda$ . In addition, the magnitudes of the matrix elements that scatter such particles decrease as well [50].

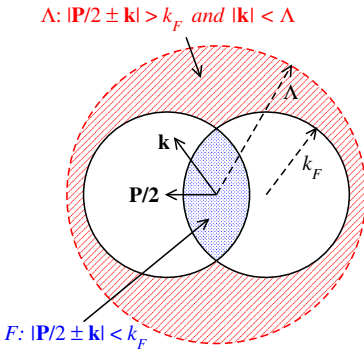


Figure 40: Overlapping Fermi spheres showing available phase space for two nucleons excited above the Fermi surface [50].

Perturbation theory in the particle-particle channel is shown in Fig. 41 for the high-resolution Argonne  $v_{18}$  potential initially and after evolution by the  $V_{\text{low } k}$  RG to low resolution ( $\Lambda = 1.9 \text{ fm}^{-1}$ ). Whereas many-body perturbation theory (MBPT) manifestly diverges for the

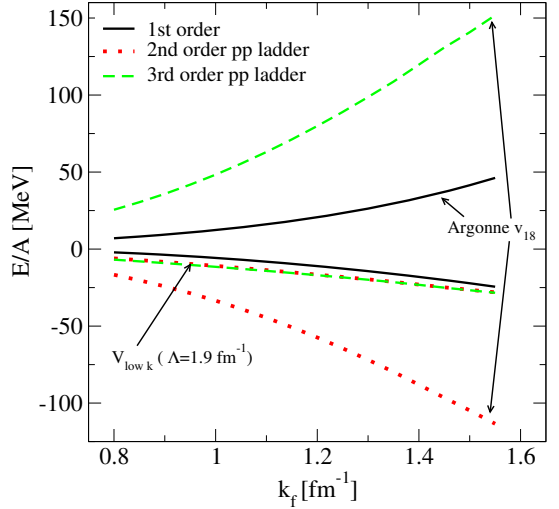


Figure 41: Many-body perturbation theory for symmetric nuclear matter up to third order in the particle-particle channel [33].

original potential, it converges for the low-momentum interaction at second order (at least in this channel; more complete many-body approximations must be studied to be more definite). It is also evident that there is no saturation. But adding a 3NF fit only to few-body properties, as in Fig. 42, shows that the empirical saturation point can be reproduced with an uncertainty of about 2–3 MeV/particle. On-going work to improve this result includes the development of SRG evolution for the 3NF in momentum space [37] and of coupled cluster methods for infinite matter with 3NF's to provide a high-order resummation of perturbation theory to test convergence.

### 4.3. Universality from flow equations

Another general aspect of RG flows known from the study of critical phenomena is the appearance of universal behavior. In the application of RG to nuclear interactions, the universality we observe is that distinct initial NN potentials that reproduce the experimental low-energy scattering phase shifts, are found to collapse to a single universal potential. We've already seen an indication of this, but here we document it in more detail.

We focus on the SRG, but very similar conclusions are found for  $V_{\text{low } k}$  evolution. In Figs. 43 and 44, S-wave N<sup>3</sup>LO chiral EFT potentials from Refs. [29] and [51] are evolved with the SRG. Although the level of truncation is the same and the cutoffs approximately equal, the methods of regulating the potential differ (particularly for the two-pion exchange part). The result is very different looking initial interactions. This is not

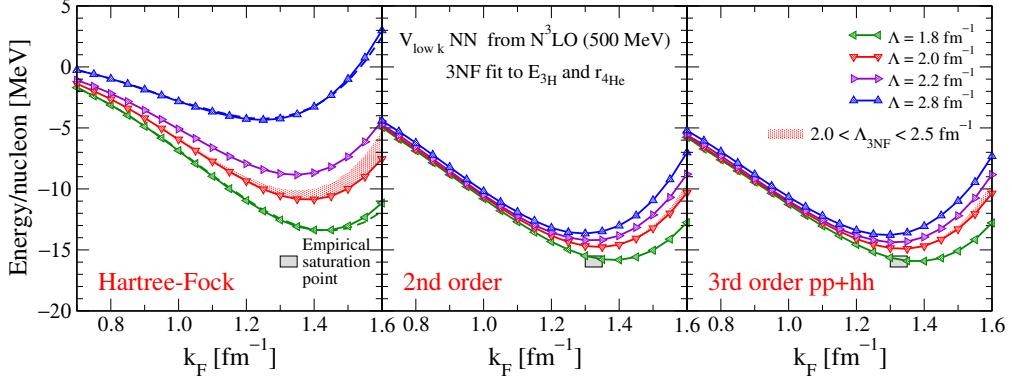


Figure 42: Many-body perturbation theory calculations of symmetric nuclear matter with  $V_{\text{low } k}$  NN potentials at four different cutoffs and the leading-order 3NF from chiral EFT [33]. The two free parameters in the 3NF are fit at each density to the triton binding energy and the alpha particle radius.

a concern, because the NN potential is not an observable. We also observe there is significant off-diagonal strength coupling low and medium momenta in the initial potentials.

As the potentials are evolved, we see the characteristic driving toward the diagonal, with the diagonal width in  $k^2$  given roughly by  $\lambda^2$ . At the end of the evolution shown, the interactions still look quite different at first glance. However, if we focus on the low-momentum region, where  $k^2 < 2 \text{ fm}^{-2}$ , they appear much more similar. We can quantify this by taking a slice along the edge (i.e.,  $V(k, 0)$ ) and along the diagonal (i.e.,  $V(k, k)$ ) and plot these quantities for these potentials and two additional ones. This is done in Fig. 45. We see a dramatic collapse of the interaction between  $\lambda = 5 \text{ fm}^{-1}$  and  $\lambda = 2 \text{ fm}^{-1}$  for the region of  $k$  below  $\lambda$  (or maybe  $3/4 \lambda$ ). An open question under active investigation is whether evolved 3NF interactions will be universal.

#### 4.4. Operator evolution via flow equations

We have focused almost exclusively on the evolution of the Hamiltonian, but an RG transformation will also change the operators associated with measurable quantities. It is essential to be able to start with operators consistent with the Hamiltonian and then to evolve them maintaining this consistency. The first step is a prime motivation for using EFT; we will assume that we have consistent initial operators in hand. The second step can be technically difficult, especially since we will inevitably induce many-body operators as we evolve (for the same arguments as we made for the Hamiltonian). This is where the SRG is particularly advantageous, because it is technically feasible to evolve operators along with the Hamiltonian.

The SRG evolution with  $s$  (recall  $s = 1/\lambda^4$ ) of any operator  $O$  is given by:

$$O_s = U_s O U_s^\dagger , \quad (50)$$

so  $O_s$  evolves via

$$\frac{dO_s}{ds} = [[G_s, H_s], O_s] , \quad (51)$$

where we use the same  $G_s$  to evolve the Hamiltonian and all other operators. While we can directly evolve any operator like this in parallel to the evolution of the Hamiltonian, in practice it is more efficient and numerically robust to either evolve the unitary transformation  $U_s$  itself:

$$\frac{dU_s}{ds} = \eta_s U_s = [G_s, H_s] U_s , \quad (52)$$

with initial value  $U_{s=0} = 1$ , or calculate it directly from the eigenvectors of  $H_{s=0}$  and  $H_s$ :

$$U_s = \sum_i |\psi_i(s)\rangle \langle \psi_i(0)| . \quad (53)$$

Then any operator is directly evolved to the desired  $s$  by applying Eq. (50) as a matrix multiplication. The second method works well in practice.

To simplify our study of operator evolution, we consider the simplest possible operator: the momentum number operator  $a_q^\dagger a_q$ . In Fig. 46, we show the momentum distribution in the deuteron, i.e.,  $\langle \psi_d | a_q^\dagger a_q | \psi_d \rangle$  for two different realistic potentials, AV18 and CD-Bonn. As implied by the y-axis label, the momentum distribution is just the square of the deuteron wave function in momentum space. The results for the two potentials

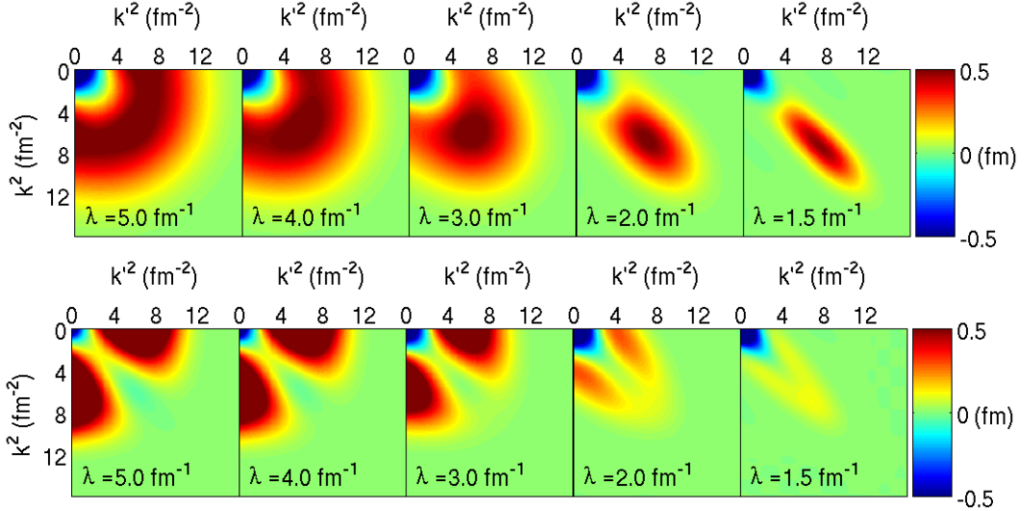
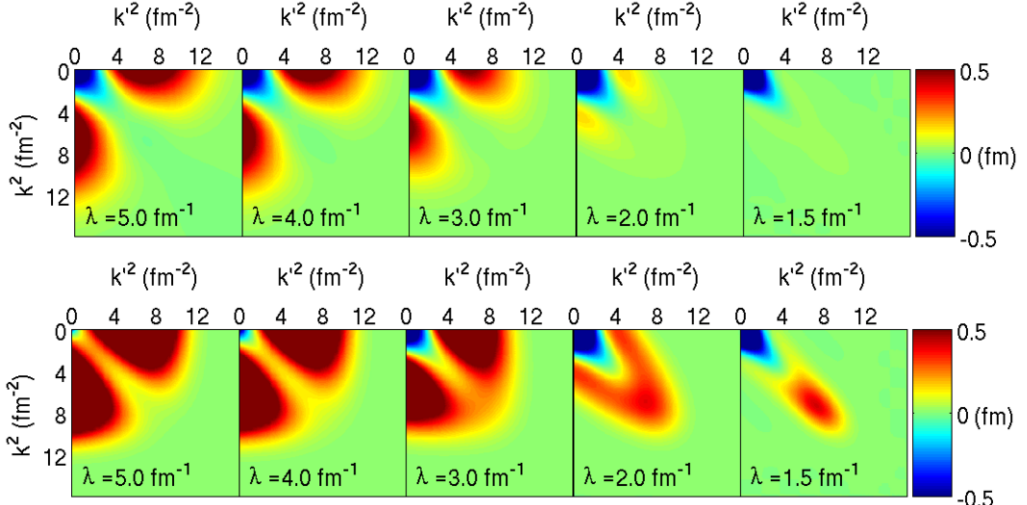
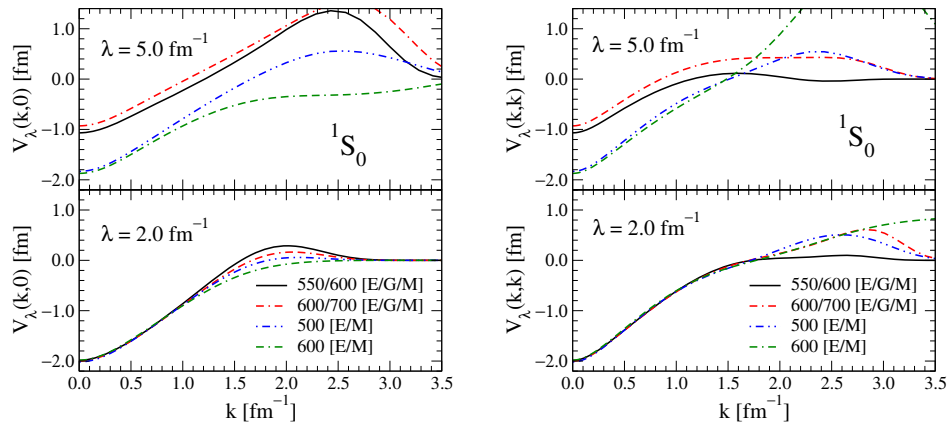
Figure 43: SRG evolution of two chiral EFT potentials in the  $^1S_0$  channel [2].Figure 44: SRG evolution of two chiral EFT potentials in the  $^3S_1$  channel [2].

Figure 45: SRG flow toward universality for several chiral EFT potentials [2].

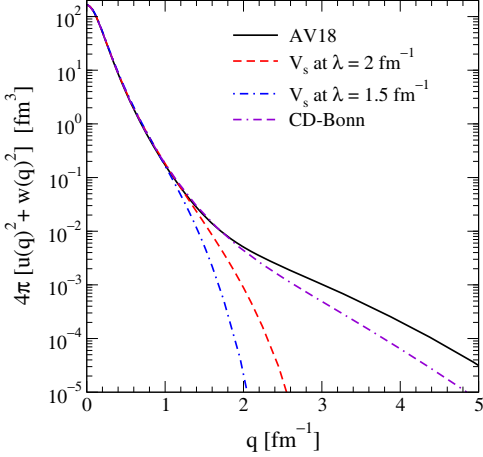


Figure 46: Momentum distribution of the deuteron for the AV18 potential and CD-Bonn potentials, compared to results from SRG potentials evolved to  $\lambda = 2.0 \text{ fm}^{-1}$  and  $1.5 \text{ fm}^{-1}$ .

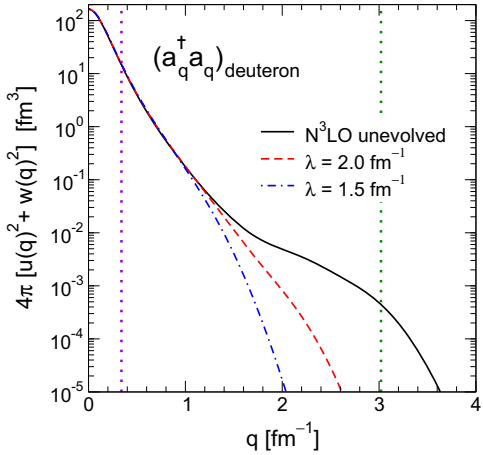


Figure 47: Momentum distribution for an unevolved chiral  $N^3\text{LO}$  potential compared to results from SRG potentials evolved to  $\lambda = 2.0 \text{ fm}^{-1}$  and  $1.5 \text{ fm}^{-1}$  [52].

agree up to about  $2 \text{ fm}^{-1}$  and then are different. If we evolve the AV18 potential *and* the momentum operator, then the matrix element  $\langle \psi_d^\lambda | O_\lambda | \psi_d^\lambda \rangle$  will be the same for any  $\lambda$  and the curve will exactly reproduce the AV18 deuteron momentum distribution. However, if we calculate  $\langle \psi_d^\lambda | a_q^\dagger a_q | \psi_d^\lambda \rangle$  for  $\lambda = 2 \text{ fm}^{-1}$  and  $1.5 \text{ fm}^{-1}$ , that is, we use the evolved wave function but the unevolved operator, then we get the other curves. Besides directly illustrating that the high- $q$  part of the momentum distribution is not an observable, since we can change it at will by unitary transformations, this manifests that the high-momentum part of the wave function is removed.

The latter is potentially disturbing, because if the evolved operator is supposed to reproduce a high momentum result when the evolved wave function has a vanishingly small component at that momentum, this may be because the operator is becoming pathological. To explore this further, we consider the momentum distribution in Fig. 47 at low ( $q = 0.34 \text{ fm}^{-1}$ ) and moderately high ( $q = 3.0 \text{ fm}^{-1}$ ) values of the momentum [52]. In Fig. 48 we plot the *integrand* of

$$\langle \psi_d^\lambda | (U a_q^\dagger a_q U^\dagger) | \psi_d^\lambda \rangle , \quad (54)$$

at each of these two  $q$  values. The full integral is the momentum distribution at those  $q$ 's, so the plots tell us where the strength of the operator lies. For the low-momentum operator, there is little renormalization, but the nature of the high-momentum operator changes completely. Originally, the integral comes entirely from the region of  $q = 3.0 \text{ fm}^{-1}$ , but the evolution of the operator shifts its strength entirely to low momentum. This result is similar for other operators, such as electromagnetic form factors [52].

As we move to  $A \geq 3$ , the operator evolution and extraction process becomes more involved. A flowchart for the procedure is given in Fig. 49. Imagine we initially have a one-body operator and we want to evolve and then evaluate it in an  $A$ -particle nucleus. The difficulty is that  $n$ -body components are induced as we evolve and these must be separated out so we can correctly embed them in the nucleus. In particular, to embed an  $n$ -body operator in an anti-symmetrized  $A$ -particle nucleus, we need an embedding factor of  $\binom{A}{n}$ , so we need to isolate the components first.

With the usual SRG generators, there is no evolution of one-body operators. This is easiest to see in second quantization, where the commutators on the right side yield operators that have at least four creation/destruction operators, meaning it is two- and higher-body. To isolate the two-body part, we first evolve the Hamiltonian in the two-particle basis to find the unitary operator  $U_s^{(2)}$  and use it to evolve our operator. Then if we subtract the embedded one-body operator, we will have our two-body part. The one- and two-body parts are then embedded in the 3-particle basis and subtracted from the evolved operator in that basis. And so on until we reach the desired level of truncation, at which point we embed in the  $A$ -particle basis and perform the  $A$ -particle calculation. More details and examples can be found about operator evolution in Ref. [52].

#### 4.5. Computational aspects

Before concluding this lecture, we'd like to make some brief comments on the computational aspects of

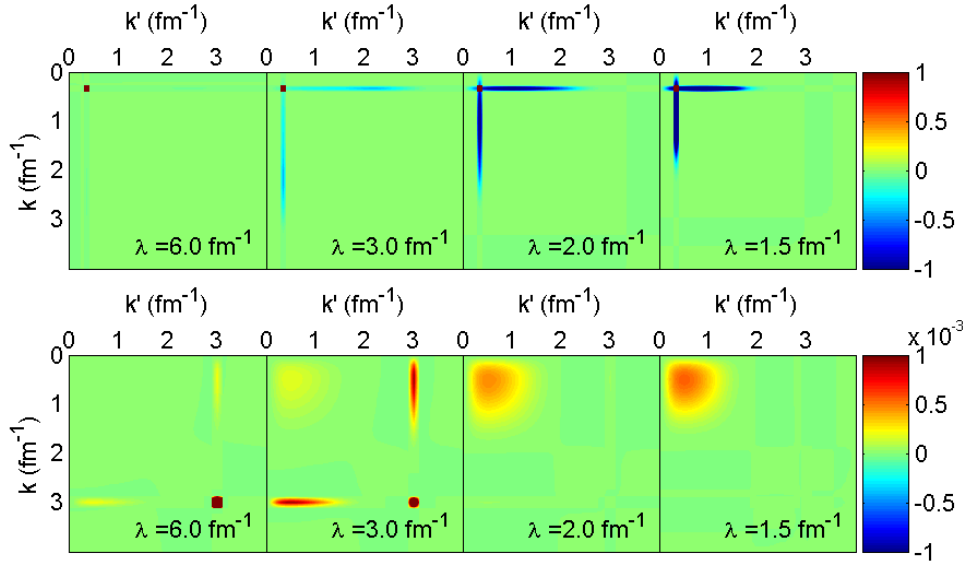


Figure 48: Integrand of momentum distribution operator [52].

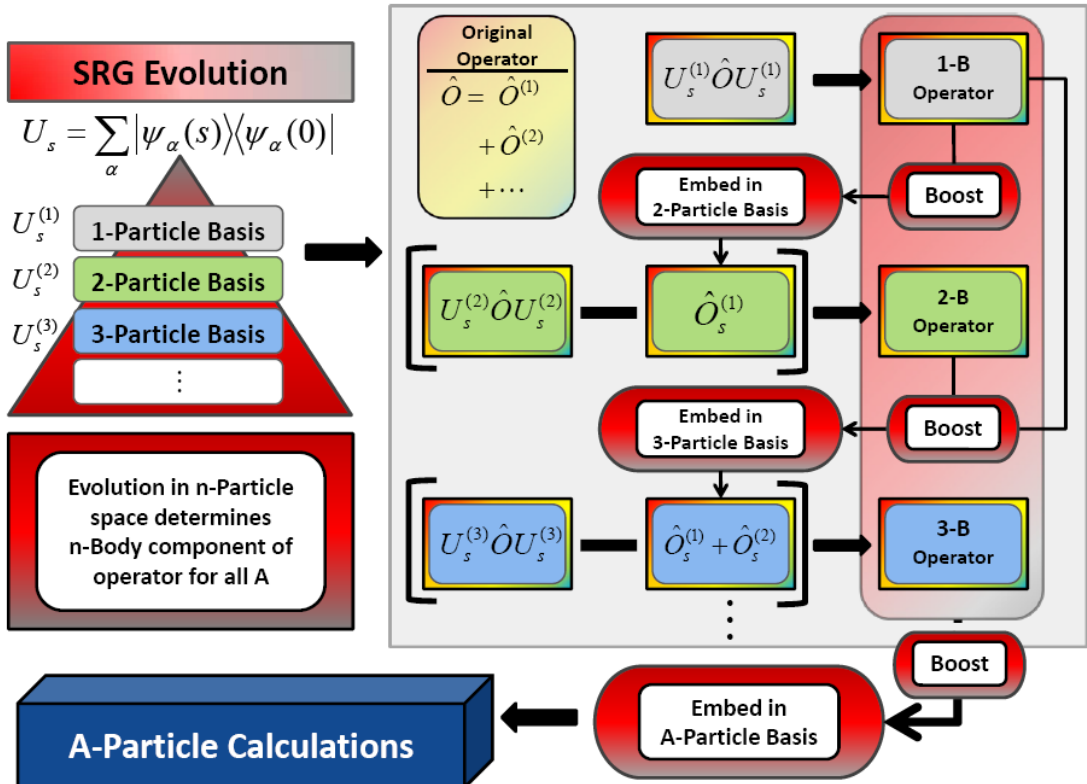


Figure 49: Schematic of the SRG operator evolution and embedding process [53].

the calculations behind the figures we've seen. As noted earlier, the continuous momentum is discretized into a finite number of momentum points. The subsequent discretization of integrals leads directly to matrices, and most of the manipulations are efficiently cast in this language. For example, momentum-space flow equations have integrals like:

$$I(p, q) \equiv \int dk k^2 V(p, k) V(k, q). \quad (55)$$

The usual choice of discretization is to use gaussian quadrature to accurately evaluate integrals with a minimum of points. (The size is not an issue for two-body operators, but becomes critical for higher-body operators.) We introduce gaussian nodes and weights  $\{k_n, w_n\}$  with  $(n = 1, N)$  to reduce integrals to finite sums:

$$\int dk f(k) \approx \sum_n w_n f(k_n). \quad (56)$$

(Note: these sets of nodes and weights are generally a combination of separate smaller rules over adjacent intervals with a *total* of  $N$  points.) Then  $I(p, q) \rightarrow I_{ij}$ , where  $p = k_i$  and  $q = k_j$ , and

$$I_{ij} = \sum_n k_n^2 w_n V_{in} V_{nj} \rightarrow \sum_n \tilde{V}_{in} \tilde{V}_{nj} \quad (57)$$

where

$$\tilde{V}_{ij} \equiv \sqrt{w_i} k_i V_{ij} k_j \sqrt{w_j}. \quad (58)$$

This allows us to solve SRG equations and integral equations for phase shifts, Schrödinger equation in momentum representation. In practice,  $N \approx 100$  gauss points is adequate for accurate nucleon-nucleon partial waves.

A computer code that carries out SRG evolution can be remarkable simple. Here is a possible pseudocode that is suitable:

1. Set up basis (e.g., momentum grid with gaussian quadrature or HO wave functions with  $N_{\max}$ )
2. Calculate (or input) the initial Hamiltonian and  $G_s$  matrix elements (including any weight factors)
3. Reshape the right side  $[[G_s, H_s], H_s]$  to a vector and pass it to a coupled differential equation solver
4. Integrate  $V_s$  to desired  $s$  (or  $\lambda = s^{-1/4}$ )
5. Diagonalize  $H_s$  with standard symmetric eigen-solver  $\Rightarrow$  energies and eigenvectors
6. Form  $U = \sum_i |\psi_s^{(i)}\rangle\langle\psi_s^{(i)}|$  from the eigenvectors
7. Output or plot or calculate observables

Such a code has been implemented in MATLAB, Mathematica, Python, C++, and Fortran-90. While any basis can be used, so far only discretized momentum and harmonic oscillator bases have been implemented. Note that the same procedure (and even the same code in some cases) is relevant for a many-particle basis, but the number of differential equations will grow rapidly. For accurate results in the two-body evolution,  $100^2 = 10,000$  matrix elements are needed, so there are that many differential equations. For an accurate 3NF evolution in a harmonic oscillator basis, at least 20 million coupled differential equations need to be solved. This sounds intimidating, but is well within reach of MATLAB (for example) on a machine with a moderate amount of memory.

#### 4.6. Summary points

Chiral EFT establishes a hierarchy of many-body forces. Using flow equations to run to low resolution makes many-body calculations more perturbative and interactions flow to universal form (at least for NN; this is not yet established for the 3NF). Operators can be evolved consistently with interaction. Long-distance operators change very little, while short-distance operators renormalize significantly, accompanied in some cases by a change in physics interpretation. The basic SRG flow equations in a partial wave momentum basis can be cast in a form that involves just matrix manipulations and the solution of ordinary first-order, coupled differential equations.

### 5. Nuclear applications and open questions

In this final lecture, we take a look at the in-medium similarity renormalization group (IM-SRG) and make a broad survey of nuclear applications. We conclude with a summary of open problems and new challenges.

#### 5.1. In-medium similarity renormalization group

We start with a review of Hartree-Fock. The Hartree-Fock wave function is the best single Slater determinant

$$|\Psi_{\text{HF}}\rangle = \det\{\phi_i(\mathbf{x}), i = 1 \dots A\}, \quad \mathbf{x} = (\mathbf{r}, \sigma, \tau) \quad (59)$$

in the variational sense. The  $\phi_i(\mathbf{x})$  single-particle wave functions satisfy *non-local* Schrödinger equations:

$$-\frac{\nabla^2}{2M} \phi_i(\mathbf{x}) + V_{\text{H}}(\mathbf{x}) \phi_i(\mathbf{x}) + \int dy V_{\text{E}}(\mathbf{x}, \mathbf{y}) \phi_i(\mathbf{y}) = \epsilon_i \phi_i(\mathbf{x}) \quad (60)$$

with direct

$$V_H(\mathbf{x}) = \int dy \sum_{j=1}^A |\phi_j(\mathbf{y})|^2 \mathbf{v}(\mathbf{x}, \mathbf{y}) \quad (61)$$

and exchange

$$V_E(\mathbf{x}, \mathbf{y}) = -v(\mathbf{x}, \mathbf{y}) \sum_{j=1}^A \phi_j(\mathbf{x}) \phi_j^*(\mathbf{y}) \quad (62)$$

potentials [54, 55]. The direct and exchange potentials are shown diagrammatically in Fig. 50, with the right-most diagram an abbreviated form called a Hugenholtz diagram [56]. We must solve self-consistently using occupied orbitals for  $V_H$  and  $V_E$ . Then Slater determinants from all orbitals form an  $A$ -body basis.



Figure 50: Feynman and Hugenholtz diagrams for Hartree-Fock.

The in-medium SRG (IM-SRG) for nuclei, developed recently by Tsukiyama, Bogner, and Schwenk [57], applies the flow equations in an  $A$ -body system using a different reference state than the vacuum. For example, we can choose the Hartree-Fock ground state as a reference state. The appealing consequence is that, unlike the free-space SRG evolution, the in-medium SRG can approximately evolve 3, ...,  $A$ -body operators using only two-body machinery. However, also in contrast to the free-space SRG, the in-medium evolution must be repeated for each nucleus or density.

The key to the IM-SRG simplification is the use of *normal-ordering* with respect to a finite-density reference state. That is, starting from the second-quantized Hamiltonian with two- and three-body interactions,

$$\begin{aligned} H = & \sum_{12} T_{12} a_1^\dagger a_2 + \frac{1}{(2!)^2} \sum_{1234} \langle 12|V|34\rangle a_1^\dagger a_2^\dagger a_4 a_3 \\ & + \frac{1}{(3!)^2} \sum_{123456} \langle 123|V^{(3)}|456\rangle a_1^\dagger a_2^\dagger a_3^\dagger a_6 a_5 a_4, \end{aligned} \quad (63)$$

all operators are normal-ordered with respect to a finite-density Fermi vacuum  $|\Phi\rangle$  (for example, the Hartree-Fock ground state or the non-interacting Fermi sea in nuclear matter), as opposed to the zero-particle vacuum.

Wick's theorem can then be used to *exactly* write  $H$  as

$$\begin{aligned} H = & E_0 + \sum_{12} f_{12} \{a_1^\dagger a_2\} \\ & + \frac{1}{(2!)^2} \sum_{1234} \langle 12|\Gamma|34\rangle \{a_1^\dagger a_2^\dagger a_4 a_3\} \\ & + \frac{1}{(3!)^2} \sum_{123456} \langle 123|\Gamma^{(3)}|456\rangle \{a_1^\dagger a_2^\dagger a_3^\dagger a_6 a_5 a_4\}, \end{aligned} \quad (64)$$

where the zero-, one-, and two-body normal-ordered terms are given by

$$\begin{aligned} E_0 = & \langle \Phi | H | \Phi \rangle = \sum_1 T_{11} n_1 \\ & + \frac{1}{2} \sum_{12} \langle 12 | V | 12 \rangle n_1 n_2 \\ & + \frac{1}{3!} \sum_{123} \langle 123 | V^{(3)} | 123 \rangle n_1 n_2 n_3, \end{aligned} \quad (65)$$

$$\begin{aligned} f_{12} = & T_{12} + \sum_i \langle 1i | V | 2i \rangle n_i \\ & + \frac{1}{2} \sum_{ij} \langle 1ij | V^{(3)} | 2ij \rangle n_i n_j, \end{aligned} \quad (66)$$

$$\langle 12|\Gamma|34\rangle = \langle 12|V|34\rangle + \sum_i \langle 12i|V^{(3)}|34i\rangle n_i, \quad (67)$$

and  $n_i = \theta(\epsilon_F - \epsilon_i)$  denotes the sharp occupation numbers in the reference state, with Fermi level or Fermi energy  $\epsilon_F$ .

By construction, the normal-ordered strings of creation and annihilation operators obey  $\langle \Phi | \{a_1^\dagger \cdots a_n\} | \Phi \rangle = 0$ . It is evident from Eqs. (65)–(67) that the coefficients of the normal-ordered zero-, one-, and two-body terms include contributions from the three-body interaction  $V^{(3)}$  through sums over the occupied single-particle states in the reference state  $|\Phi\rangle$ . Therefore, truncating the in-medium SRG equations to two-body *normal-ordered* operators will (approximately) evolve induced three- and higher-body interactions through the density-dependent coefficients of the zero-, one-, and two-body operators in Eq. (64).

The in-medium SRG flow equations at the normal-ordered two-body level are obtained by evaluating  $dH/ds = [\eta, H]$  with the normal-ordered Hamiltonian  $H = E_0 + f + \Gamma$  and the SRG generator  $\eta = \eta^{1b} + \eta^{2b}$  (with one- and two-body terms) and neglecting three- and higher-body normal-ordered terms. For infinite matter, a natural generator choice is  $\eta = [f, \Gamma]$  in analogy with the free-space SRG. In this case, the explicit form of the SRG equations simplifies because  $\eta^{1b} = 0$  and

$f_{ij} = f_i \delta_{ij}$ . This leads to

$$\frac{dE_0}{ds} = \frac{1}{2} \sum_{1234} (f_{12} - f_{34}) |\Gamma_{1234}|^2 n_1 n_2 \bar{n}_3 \bar{n}_4, \quad (68)$$

$$\begin{aligned} \frac{df_1}{ds} &= \sum_{234} (f_{41} - f_{23}) |\Gamma_{4123}|^2 \\ &\times (\bar{n}_2 \bar{n}_3 n_4 + n_2 n_3 \bar{n}_4), \end{aligned} \quad (69)$$

$$\begin{aligned} \frac{d\Gamma_{1234}}{ds} &= -(f_{12} - f_{34})^2 \Gamma_{1234} \\ &+ \frac{1}{2} \sum_{ab} (f_{12} + f_{34} - 2f_{ab}) \Gamma_{12ab} \Gamma_{ab34} \\ &\times (1 - n_a - n_b) \\ &+ \sum_{ab} (n_a - n_b) \\ &\times \left\{ \Gamma_{a1b3} \Gamma_{b2a4} [(f_{a1} - f_{b3}) - (f_{b2} - f_{a4})] \right. \\ &\left. - \Gamma_{a2b3} \Gamma_{b1a4} [(f_{a2} - f_{b3}) - (f_{b1} - f_{a4})] \right\}, \end{aligned} \quad (70)$$

where the single-particle indices refer to momentum states and include spin and isospin labels.

While the in-medium SRG equations are of second order in the interactions, the flow equations build up non-perturbative physics via the successive interference between the particle-particle and the two particle-hole channels in the SRG equation for  $\Gamma$ , Eq. (70), and between the two-particle-one-hole and two-hole-one-particle channels for  $f$ , Eq. (69). In terms of diagrams, one can imagine iterating the SRG equations in increments of  $\delta s$ . At each additional increment  $\delta s$ , the interactions from the previous step are inserted back into the right side of the SRG equations. Iterating this procedure, one sees that the SRG accumulates complicated particle-particle and particle-hole correlations to all orders.

With the choice of generator  $\eta = [f, \Gamma]$ , the Hamiltonian is driven towards the diagonal. This means that Hartree-Fock becomes increasingly dominant with the off-diagonal  $\Gamma$  matrix elements being driven to zero. As with the free-space SRG, it is convenient for momentum-space evolution to switch to the flow variable  $\lambda \equiv s^{-1/4}$ , which is a measure of the resulting band-diagonal width of  $\Gamma$ . In the limit  $\lambda \rightarrow 0$ , Hartree-Fock becomes exact for the evolved Hamiltonian; the zero-body term,  $E_0$ , approaches the interacting ground-state energy,  $f$  approaches fully dressed single-particle energies, and the remaining diagonal matrix elements of  $\Gamma$  approach a generalization of the quasiparticle interaction in Landau's theory of Fermi liquids [1].

An approximate solution of the  $E_0$  flow equation for

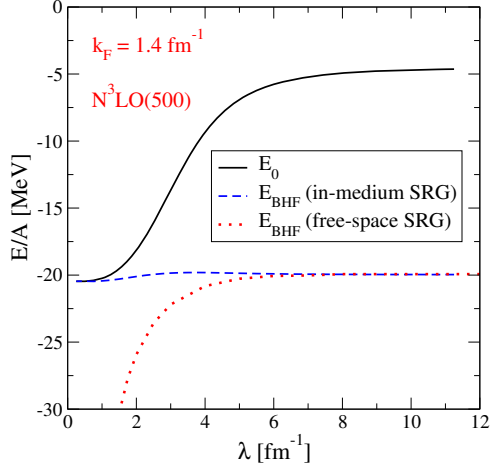


Figure 51: Symmetric nuclear matter energy/particle at  $k_F = 1.4 \text{ fm}^{-1}$  as evolved in the IM-SRG [57].

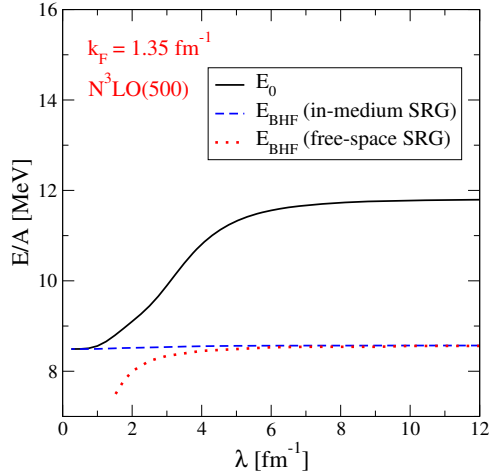


Figure 52: Neutron matter energy/particle at  $k_F = 1.35 \text{ fm}^{-1}$  as evolved in the IM-SRG [57].

symmetric nuclear matter and neutron matter as a function of  $\lambda$  is shown in Figs. 51 and 52 for two different Fermi momenta  $k_F$  (corresponding to different densities). As expected, the in-medium SRG drives the Hamiltonian to a form where Hartree-Fock becomes exact in the limit  $\lambda \rightarrow 0$ . In contrast to the ladder approximation based on NN-only SRG interactions evolved in free space, the same many-body calculation using interactions evolved with the in-medium SRG at the two-body level gives energies that are approximately independent of  $\lambda$ . This indicates that truncations based on normal-ordering efficiently include the dominant induced many-body interactions via the density-

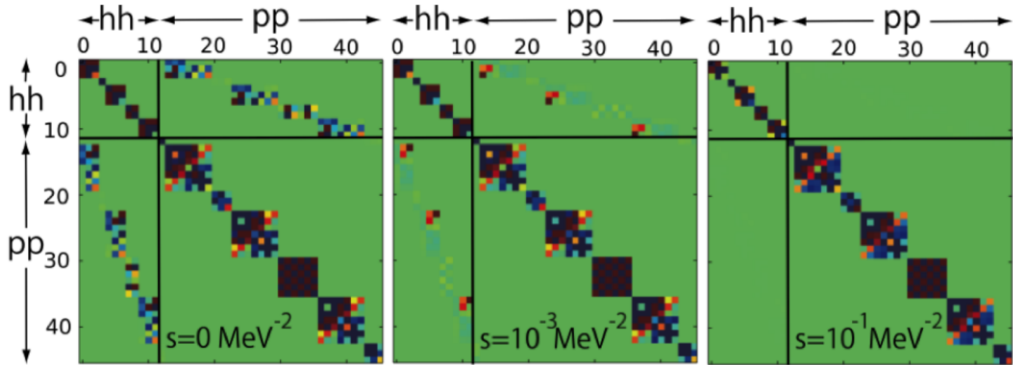


Figure 53: “Off-diagonal” terms (e.g.,  $2p2h$  sectors) driven to zero as  $s$  increases, decoupling them from the Hartree-Fock reference state, which becomes exact as  $s \rightarrow \infty$  [57].

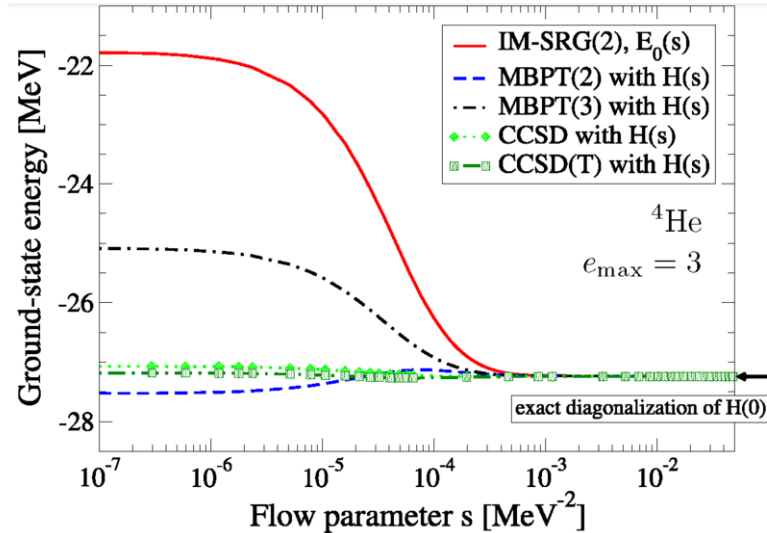


Figure 54: IM-SRG flow for the energy of the alpha particle [57].

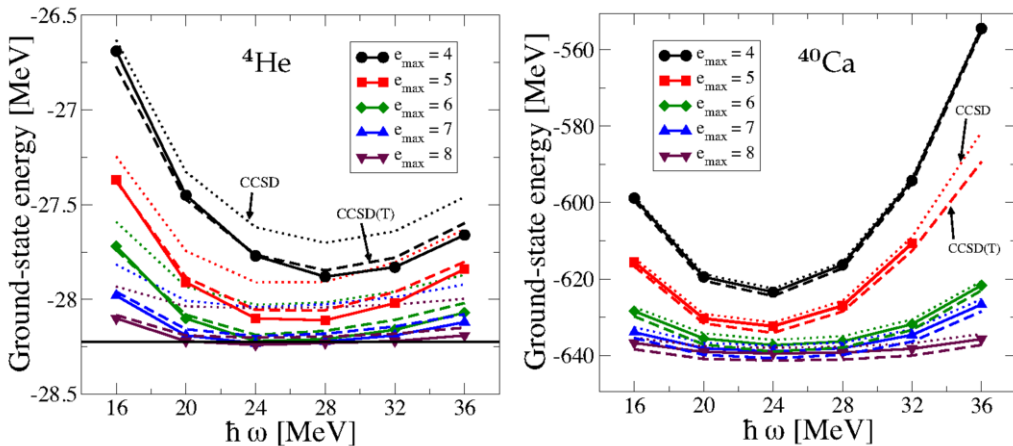


Figure 55: IM-SRG convergence in finite nuclei compared to coupled cluster CCSD and CCSD(T) calculations [57].

dependent zero-, one-, and two-body normal-ordered terms.

In a similar manner, the in-medium SRG can be used as an ab initio method for finite nuclei. Figure 53 shows the off-diagonal normal-ordered two-body matrix elements  $\Gamma$  being driven to zero with the IM-SRG evolution. Figure 54 shows the evolution of the ground-state energy of  ${}^4\text{He}$  [57]. As the flow parameter  $s$  increases, the  $E_0$  flow and second-order (in  $\Gamma$ ) many-body perturbation theory contributions approach each other, as was the case for the infinite matter results in Fig. 51. In addition, the convergence behavior with increasing harmonic-oscillator spaces in Fig. 55 for  ${}^4\text{He}$  and  ${}^{40}\text{Ca}$  is very promising. Based on these calculations, the in-medium SRG truncated at the normal-ordered two-body level appears to give accuracies comparable to coupled-cluster calculations truncated at the singles and doubles (CCSD) level. Finally, we note that the in-medium SRG is a promising method for non-perturbative calculations of valence shell-model effective interactions and operators.

## 5.2. Implications of RG for nuclear calculations

There are many on-going and potential applications of low resolution methods for calculations of nuclear structure and reactions. In many cases RG techniques are used explicitly but there are also examples of low resolution being achieved by other means. Here we'll survey some of both types. This will be far from a comprehensive list because it focuses largely on developments associated entirely or in part with a project called UNEDF, which stands for Universal Nuclear Energy Density Functional.

UNEDF is a collaboration of more than fifty physicists, applied mathematicians, and computer scientists in the United States plus many international collaborators, funded through the U.S. Department of Energy's SciDAC program. The long-term vision of the project is to arrive at a comprehensive and quantitative description of nuclei and their reactions. The focused mission is to construct, optimize, validate, and apply energy density functionals for structure and reactions, but to carry out this mission the team has developed many crosscutting physics collaborations where none existed previously between the main physics areas: ab initio structure, ab initio functionals, DFT applications, DFT extensions, reactions. These interconnections are indicated schematically in the UNEDF strategy diagram in Fig. 56. This type of large-scale collaboration represents a transformation in how low-energy nuclear theory is done. UNEDF has been very productive, with

over 200 publications to date, including 11 Physical Review Letters and a Science article in the 2011 calendar year alone. Further background, references, and scientific highlights can be found at unedf.org, the project website.

One of the important tools for nuclear structure enabled by low-resolution interactions is the diagonalization of enormous but very sparse Hamiltonian matrices, usually in a harmonic oscillator basis to permit center-of-mass effects to be excluded. This is referred to as no-core full configuration (NCFC) or no-core shell model (NCSM), depending on the context. Two recent examples of what is enabled are represented in Fig. 57. On the left are Gamov-Teller matrix elements from a large-scale calculation of Carbon-14 using a soft chiral EFT potential [58]. They highlight the critical role of the 3NF in suppressing the beta decay rate, which explains the anomalously long lifetime of  ${}^{14}\text{C}$  (which is used to great advantage for dating artifacts!). On the right is the low-lying spectrum of Fluorine-14, which is unstable to proton decay. This spectrum was predicted in advance of the experimental measurements (not a common occurrence until now!), which meant solving a Hamiltonian matrix of dimension 2 billion using 30,000 cores with a soft interaction (derived from inverse scattering rather than RG, but with similar characteristics) [59, 60]. The predictions and measurement agree within the combined experimental and theoretical uncertainties. These calculations would not be possible with the potentials of Fig. 3. RG-softened interactions will allow many more of these confrontations of experiment with theory in the future.

One of the principal aims of the UNEDF project is to calculate reliable reaction cross sections for astrophysics, nuclear energy, and national security, for which extensions of standard phenomenology is insufficient. The interplay of structure and reactions is essential for a successful description of exotic nuclei as well. Such interplay is characteristic of the ab initio no-core shell model/resonating-group method (NCSM/RGM), which treats bound and scattering states within a unified framework using fundamental interactions between all nucleons. A quantitative proof-of-principle calculation of this approach is shown in Fig. 58 [61, 62]. A wide range of applications is now possible including  ${}^3\text{H}(d, n){}^4\text{He}$  fusion and the  ${}^7\text{Be}(p, \gamma){}^8\text{B}$  reaction important for solar neutrino physics, and many more to come. In Fig. 59, the first-ever ab-initio calculation of the  ${}^7\text{Be}(p, \gamma){}^8\text{B}$  astrophysical S-factor is shown [63]. This calculation uses NCSM/RGM with an  $N^3\text{LO}$  NN interaction evolved by the SRG to a fine-tuned value of  $\lambda = 1.86 \text{ fm}^{-1}$ . The ab initio theory predicts both the normalization and

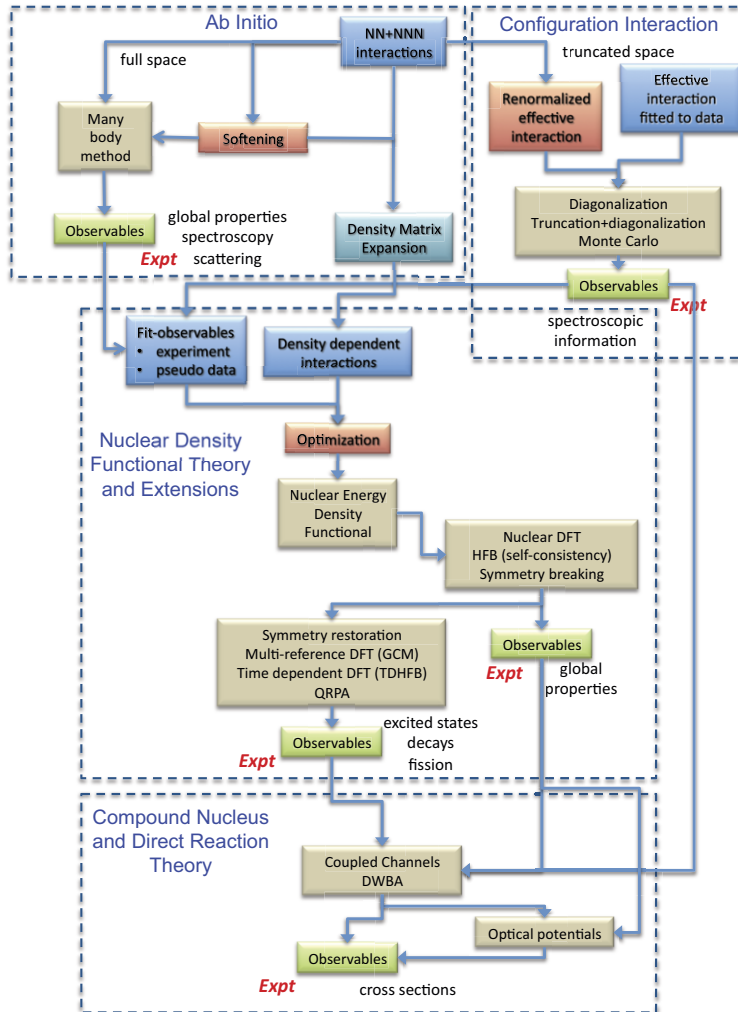


Figure 56: Strategy diagram for UNEDF.

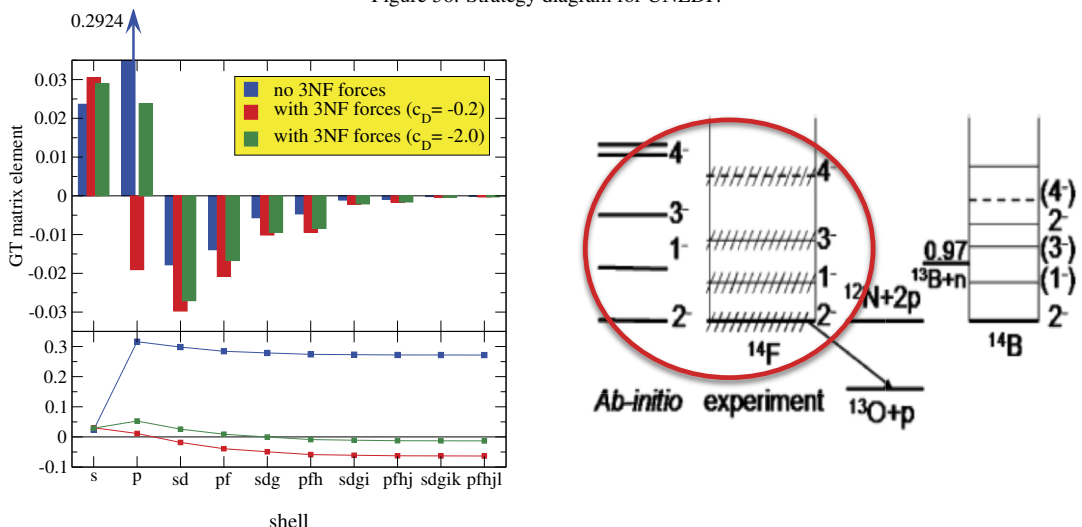


Figure 57: Left: Matrix elements from Carbon-14 lifetime calculation [58]. Right: Fluorine-14 spectrum predicted by NCSM and measured experimentally[59, 60].

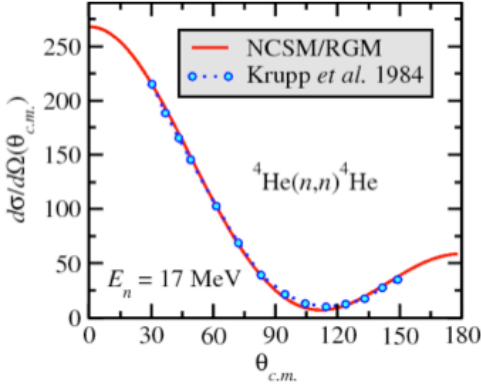


Figure 58: NCSM/RGM calculation of neutron scattering from the alpha particle using SRG-evolved interactions, compared with experimental measurements [61, 62].

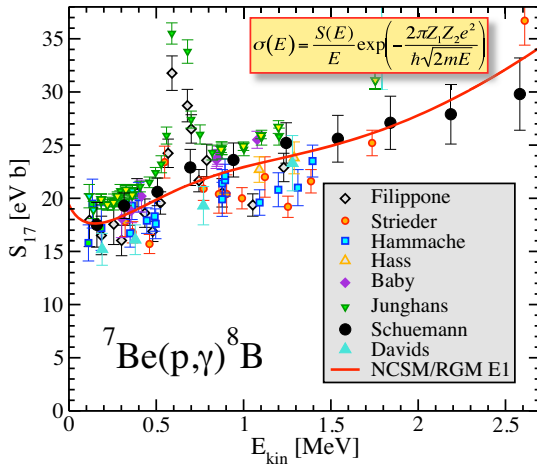


Figure 59: First ever ab initio calculations of  ${}^7\text{Be}(p,\gamma){}^8\text{B}$  astrophysical S-factor [63]. Uses SRG-N3LO with  $\lambda = 1.86 \text{ fm}^{-1}$ .

the shape of  $S_{17}$ . This very promising technique has many additional applications. The inclusion of an SRG-evolved 3NF is planned for the near future.

UNEDF members have demonstrated that the powerful coupled-cluster (CC) ab initio method, which is a workhorse in quantum chemistry, can be used to accurately calculate closed-shell medium-mass nuclei such as  ${}^{40}\text{C}$ ,  ${}^{48}\text{C}$ ,  ${}^{56}\text{Ni}$  with chiral EFT two-body interactions or the RG-softened versions [64, 65], as well as proton halo nuclei like  ${}^{19}\text{F}$  [66]. A proof-of-principle convergence curve (ground-state energy versus the size of the orbital space) for  ${}^{56}\text{Ni}$  with an SRG-evolved potential is shown in Fig. 60. The CC formalism has been extended to include NNN forces and their inclusion in calculations of the heavier nuclei will break new barriers.

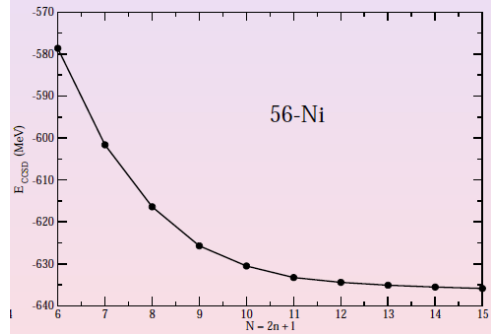


Figure 60: Convergence of CCSD for Ni-56 evolved N3LO to  $\lambda = 2.5 \text{ fm}^{-1}$ .

The in-medium SRG diagonalization of closed-shell nuclei such as  ${}^{40}\text{C}$  [57], discussed in Section 5.1 is a complementary approach to CC and is one of several advances in our understanding of the phenomenological nuclear shell model enabled by softened potentials. Another is the direct use of MBPT to examine the effect of the 3NF on the location of the neutron dripline: the limits of nuclear existence where an added neutron is no longer bound—it “drips” away. The new physics is indicated schematically in Fig. 61. It’s been established experimentally that as you add neutrons to stable oxygen-16, the neutrons stay bound until  ${}^{24}\text{O}$ . But adding one more proton to get fluorine extends the dripline all the way to  ${}^{31}\text{F}$ . This result is *not* predicted by previous microscopic calculations using NN interactions, because the single-particle neutron energy levels that get filled are predicted to be bound (leftmost panel in Fig. 62), leading to  ${}^{28}\text{O}$  as the calculated dripline. The phenomenological shell model, in which matrix elements of the Hamiltonian are fit to nearby nuclei, has a very different pattern (e.g., compare the  $d3/2$  single-particle en-

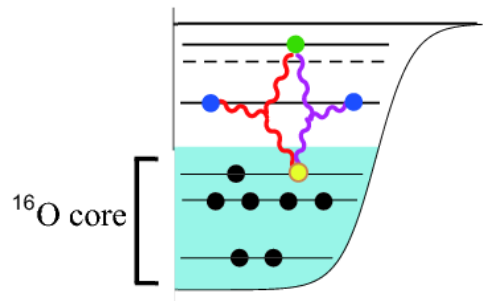


Figure 61: Influence of a three-body force on valence neutrons in oxygen isotopes.

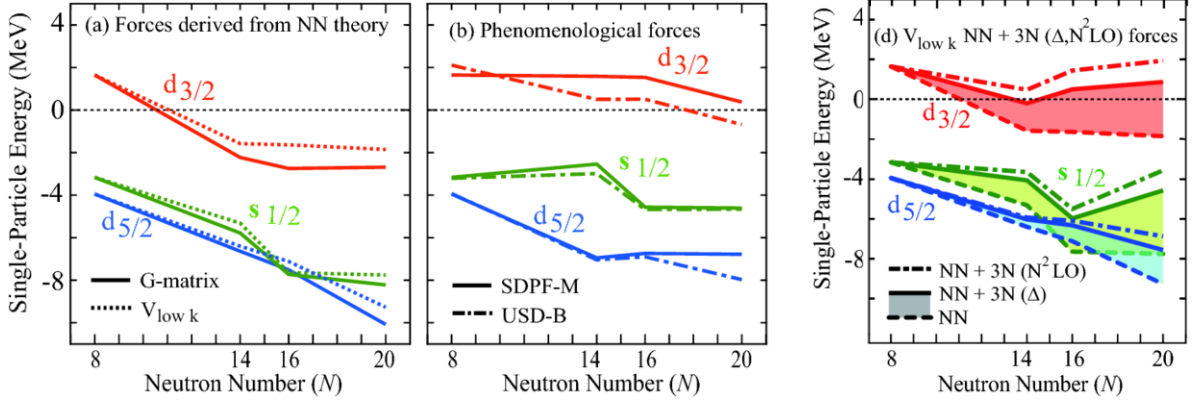


Figure 62: Three-body force impact on oxygen single-particle levels. Left: NN-only, middle: phenomenological forces, right: NN + 3NF.

ergies in the middle and left panels of Fig. 62) and predicts the correct dripline. However, recent calculations with a  $V_{\text{low } k}$  RG force and fitted 3NF yield the right panel of Fig. 62. When the 3NF effect is added [67], the interaction of valence neutrons with a core neutron, as in Fig. 61, is repulsive, pushing up the  $d_{3/2}$  level so that the dripline is at  $^{24}\text{O}$ .

The apparent success of MBPT with low-momentum potentials has been tested by Roth and collaborators [68], who have done calculations of closed shell nuclei across the mass table in second-order perturbation theory (first-order is Hartree-Fock). Results for SRG evolved interactions from an initial NN chiral EFT and including the induced 3NF show excellent independence of the flow parameter  $\lambda$  (see Fig. 63) and both the energies and radii are in good agreement with coupled

cluster results [64, 65]. However, adding a 3NF leads to large  $\lambda$  dependence. Very recent results from Roth et al. that use importance truncated NCSM as well as coupled cluster calculations show that the long-range 3NF is the source to apparent large 4NF contributions for oxygen and heavier nuclei, causing a strong dependence on the flow parameter. However, by using a lower cutoff for the initial 3NF, remarkable agreement with experimental binding energies is achieved with fits only to few-body properties [19, 41]. Work is in progress to identify SRG generators to better control the RG evolution of the initial 3NF.

We have already seen the convergence of MBPT for symmetric infinite nuclear matter. Perturbation theory is even more controlled for pure neutron matter, as illustrated in Figs. 64 and 65, where  $V_{\text{low } k}$  RG-evolved interactions and fitted 3NF's are used in calculations of the neutron matter energy per nucleon as a function of the density [69]. The cutoff dependence of the result is used to estimate the many-body uncertainty. Figure 64 shows that the 3NF contribution is important (compare to the NN-only curves) but that the dominant theoretical uncertainty is the value of the coupling constants for the long-range part of the  $N^2\text{LO}$  chiral EFT 3NF. In Fig. 65, comparisons with non-perturbative calculations demonstrate the consistency of the much easier MBPT calculations. The results for the neutron matter equation of state have been used by Hebeler et al. to provide tight constraints on neutron star masses and radii [70].

The MBPT results for infinite matter are also valuable input for work to develop a microscopic nuclear energy density functional (EDF). A key tool to incorporate microscopic input into nuclear EDF's is the density matrix expansion (DME) originally proposed by Negele and Vautherin, which has been revived and im-

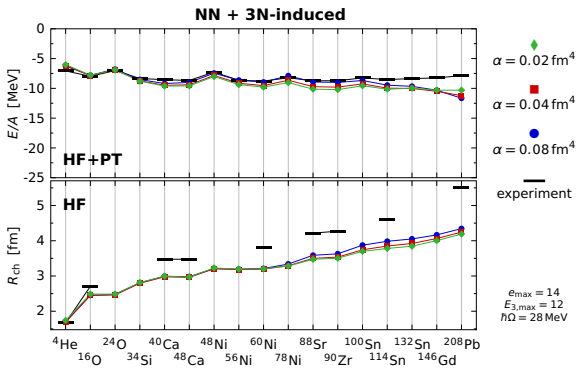


Figure 63: Second-order MBPT applied to closed shell nuclei with SRG-evolved NN interactions, including the induced 3NF [68]. Several different values of the flow parameter are shown (note that  $\alpha$  here is the same as  $s = 1/\lambda^4$ ).

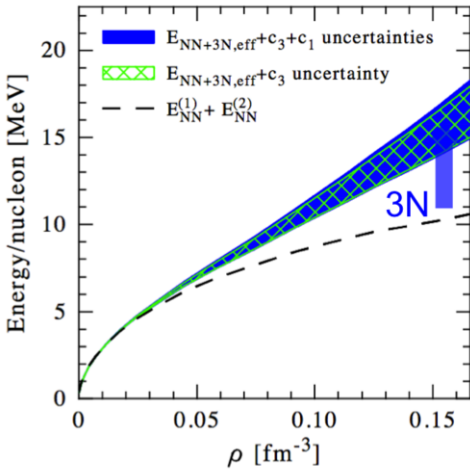


Figure 64: Neutron matter energy/particle versus density calculated using a  $V_{\text{low } k}$  RG-evolved NN interaction plus fit 3NF. The arrow shows the importance of the 3NF and the width of the band indicates the uncertainties due to 3NF couplings [69].

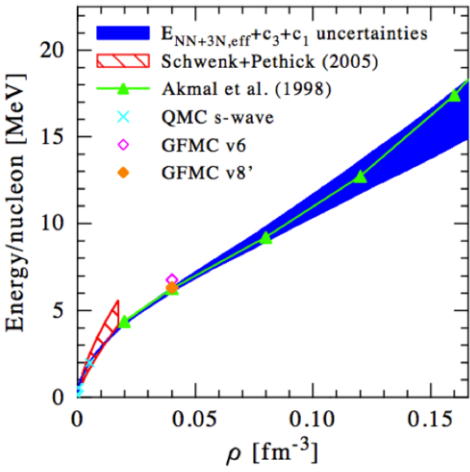


Figure 65: Neutron matter energy/particle versus density as in Fig. 64 compared to other calculations [69].

proved in the UNEDF project. The DME provides a route to an EDF based on microscopic nuclear interactions through a quasi-local expansion of the energy in terms of various local densities and currents, including resummations that can treat long-range one- and two-pion exchange interactions given by chiral EFT. With sufficiently soft microscopic interactions, many-body perturbation theory (MBPT) for nuclei is a quantitative framework for implementing the DME. The formal development of DME with MBPT is on-going, but there are already hybrid formulations between purely ab initio

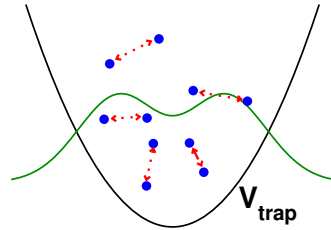


Figure 66: Schematic representation of interacting neutrons in a (theoretical) trapping potential.

tio and phenomenological functionals [71], which allow improvements to be made while more systematic functionals are developed.

Several DME implementations strategies have been developed, with the first tests recently made against ab-initio calculations using a semi-realistic interaction (Minnesota) in trapped neutron drops [72]. Neutron drops are a powerful theoretical laboratory for improving existing nuclear energy functionals, with particular value in providing microscopic input needed for neutron-rich nuclei, where there are fewer constraints from experiment. The necessity of an external potential (because the untrapped system is unbound, with positive pressure) is turned into a virtue by allowing external control over the environment (see Fig. 66 for a

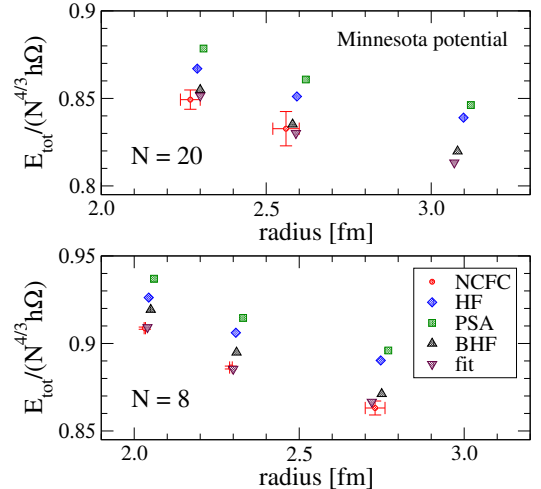


Figure 67: Calculations of the ground-state energies and radii of trapped systems of twenty (top) and eight (bottom) neutron drops [72]. The different clusters of points are for different harmonic oscillator trap frequencies. The NCFC results are exact within the error bars. They are compared to various approximate microscopic functions, with the BHF and “fit” calculations expected to be the best approximations.

schematic of the trapped neutrons). Density functional theory, which provides the theoretical underpinning for the microscopic EDF's, dictates that the same functional applies for any external potential, which can therefore be varied to probe and isolate different aspects of the EDF. Results summarized in Fig. 67 show promising agreement with the DME functionals and the (essentially exact) ab initio results using NCFC. Many more developments in this line will be forthcoming.

### 5.3. Summary and survey of open problems

In these lectures, we've made a whirlwind tour of atomic nuclei at low resolution. With the renormalization group (RG), the strategy has been to lower the resolution and track dependence on it. We've seen how high resolution leads to coupling of low momenta to high momenta, which hinders solutions of the many-body problem for low-energy properties. With RG evolution, correlations in wave functions are reduced dramatically, leading to faster convergence of many-body methods. A consequence is that non-local potentials and many-body operators are induced, so these must be accommodated.

Flow equations (SRG) achieve low resolution by *decoupling*. This can be in the form of band or block diagonalization of the Hamiltonian matrix. The flow equations implement a series of unitary transformations, in which observables (measurable quantities) are not altered but the physics interpretation can change! In the nuclear case, the usual plan is to evolve until few-body forces start to grow rapidly, or to use an in-medium version of the SRG.

With the RG, cutoff dependence becomes a new tool in low-energy nuclear physics. The basic idea is that, in principle, observables should be unchanged with RG evolution. In practice, there are approximations in the RG implementation and in calculating nuclear observables. These come from truncation or approximation of “induced” many-body forces/operators and from many-body approximations. For nuclei there can be dramatic changes even with apparently small changes in the resolution scale. We can use these changes as diagnostics of approximations and to estimate theoretical errors. Some specific applications of cutoff dependence include:

- using cutoff dependence at different orders in an EFT expansion, which carries over to the corresponding RG-evolved interactions;
- using the running of ground-state energies with cutoff in few-body systems to estimate errors and identify correlations (e.g., the Tjon line);

- in nuclear matter calculations, validating MBPT convergence and setting lower bounds on the errors from uncertainties in many-body interactions;
- in calculations of finite nuclei, diagnosing missing many-body forces;
- identifying and characterizing scheme-dependent observables, such as spectroscopic factors.

The possibilities have really only begun to be explored.

We have seen glimpses of the many promising applications of RG methods to nuclei. Configuration interaction and coupled cluster approaches using softened interactions converge faster, opening up new possibilities and allowing the limits of computational feasibility to be extended. Ground-breaking ab-initio reaction calculations are now possible. Applications of low-momentum interactions to microscopic shell model calculations bring new understanding to phenomenological results, highlighting the role of three-body forces. Because many-body perturbation theory (MBPT) is feasible with the evolved interactions, the door is opened to constructive nuclear density functional theory.

There are also many open questions and difficult problems in applying RG to low-energy nuclear physics. Here is a subset:

- Power counting for evolved many-body operators. That is, how do we anticipate the size of contributions from induced many-body interactions and other operators? This is essential if we are to have reliable estimates of theoretical errors, because truncations are unavoidable. We need both analytic estimates to guide us as well as more extensive numerical tests. Many of the same issues apply to chiral EFT; can the additional information available from SRG flow parameter dependence help with analyzing or even constructing EFT's?
- Only a few possibilities for SRG generators have been considered for nuclear systems. Can other choices for the SRG  $G_s$  operator help to control the growth of many-body forces? Can convergence be improved in the harmonic oscillator basis, which is limited by an infrared cutoff as well as an ultra-violet cutoff? Can a generator be found to drive non-local potentials to local form, so they can be used with quantum Monte Carlo methods? Or can the SRG equations be formulated to directly produce a local projection and a perturbative residual interaction?
- An apparent close connection between the block-diagonal generator SRG and the “standard”  $V_{\text{low } k}$

RG has been established empirically, but a formal demonstration of the connection and its limits has not been made.

- What other bases for SRG evolution would be advantageous? The need for a momentum-space implementation for evolution in the  $A = 3$  space and beyond is foremost. Beyond providing necessary checks of evolution in the harmonic oscillator basis, the evolved interactions in this form could be directly applied to test MBPT in infinite matter and to test nuclear scaling. Another possibility is to use hyperspherical coordinates, which combine the advantage of a discrete basis with better asymptotic behavior (and which would be useful for visualization of many-body forces).
- There are many open questions and problems involving operators. These include formal issues such as the scaling of many-body operators and technical issues such as how to handle boosts of operators that are not galilean invariant. And there are simply many applications that are yet to be made (e.g., electroweak processes).
- The flow to universal form exhibited by two-body interactions has been clear from the beginning of RG applications to nuclei, but whether this same behavior is expected for many-body interactions or for other operators is still open.
- How can we use more of the power of the RG?

There is no shortage of opportunities and challenges!

## References

- [1] S. Kehrein, The Flow Equation Approach to Many-Particle Systems, Springer, Berlin, 2006.
- [2] S. K. Bogner, R. J. Furnstahl, A. Schwenk, From low-momentum interactions to nuclear structure, *Prog. Part. Nucl. Phys.* 65 (2010) 94–147.
- [3] DOE/NSF Nuclear Science Advisory Committee, The Frontiers of Nuclear Science: A Long-Range Plan, 2007.
- [4] S. Aoki, T. Hatsuda, N. Ishii, Nuclear Force from Monte Carlo Simulations of Lattice Quantum Chromodynamics, *Comput. Sci. Dis.* 1 (2008) 015009.
- [5] R. B. Wiringa, V. G. J. Stoks, R. Schiavilla, An Accurate nucleon-nucleon potential with charge independence breaking, *Phys. Rev. C* 51 (1995) 38–51.
- [6] A. H. Guth, K. Huang, R. L. Jaffe (Eds.), Asymptotic Realms of Physics, MIT Press, Cambridge, MA, 1983.
- [7] S. K. Bogner, T. T. S. Kuo, A. Schwenk, Model-independent low momentum nucleon interaction from phase shift equivalence, *Phys. Rept.* 386 (2003) 1–27.
- [8] F. Wegner, *Ann. Phys. (Leipzig)* 3 (1994) 77.
- [9] F. J. Wegner, Flow equations for Hamiltonians, *Nucl. Phys. Proc. Suppl.* 90 (2000) 141–146.
- [10] F. Wegner, Flow equations and normal ordering: a survey, *Journal of Physics A: Mathematical and General* 39 (25) (2006) 8221–8230.
- [11] S. D. Glazek, K. G. Wilson, Renormalization of Hamiltonians, *Phys. Rev. D* 48 (1993) 5863–5872.
- [12] S. K. Bogner, R. J. Furnstahl, R. J. Perry, Similarity Renormalization Group for Nucleon-Nucleon Interactions, *Phys. Rev. C* 75 (2007) 061001.
- [13] S. K. Bogner, R. J. Furnstahl, R. J. Perry, A. Schwenk, Are low-energy nuclear observables sensitive to high-energy phase shifts?, *Phys. Lett. B* 649 (2007) 488–493.
- [14] E. D. Jurgenson, S. K. Bogner, R. J. Furnstahl, R. J. Perry, Decoupling in the Similarity Renormalization Group for Nucleon-Nucleon Forces, *Phys. Rev. C* 78 (2008) 014003.
- [15] K. Wendt, Private communication.
- [16] E. D. Jurgenson, P. Navratil, R. J. Furnstahl, Evolution of Nuclear Many-Body Forces with the Similarity Renormalization Group, *Phys. Rev. Lett.* 103 (2009) 082501.
- [17] E. Jurgenson, P. Navratil, R. Furnstahl, Evolving Nuclear Many-Body Forces with the Similarity Renormalization Group, *Phys. Rev. C* 83 (2011) 034301.
- [18] R. Roth, P. Navratil, Ab Initio Study of  $^{40}\text{Ca}$  with an Importance Truncated No-Core Shell Model, *Phys. Rev. Lett.* 99 (2007) 092501.
- [19] R. Roth, J. Langhammer, A. Calci, S. Binder, P. Navratil, Similarity-Transformed Chiral NN+3N Interactions for the Ab Initio Description of  $^{12}\text{C}$  and  $^{16}\text{O}$ , *Phys. Rev. Lett.* 107 (2011) 072501.
- [20] S. K. Bogner, R. J. Furnstahl, R. J. Perry, Three-Body Forces Produced by a Similarity Renormalization Group Transformation in a Simple Model, *Annals Phys.* 323 (2008) 1478–1501.
- [21] S. D. Glazek, R. J. Perry, The impact of bound states on similarity renormalization group transformations, *Phys. Rev. D* 78 (2008) 045011.
- [22] K. Wendt, R. Furnstahl, R. Perry, Decoupling of Spurious Deep Bound States with the Similarity Renormalization Group, *Phys. Rev. C* 83 (2011) 034005.
- [23] W. Li, E. Anderson, R. Furnstahl, The Similarity Renormalization Group with Novel Generators, *Phys. Rev. C* 84 (2011) 054002.
- [24] S. K. Bogner, R. J. Furnstahl, S. Ramanan, A. Schwenk, Low-momentum interactions with smooth cutoffs, *Nucl. Phys. A* 784 (2007) 79–103.
- [25] H. Feldmeier, T. Neff, R. Roth, J. Schnack, A unitary correlation operator method, *Nucl. Phys. A* 632 (1998) 61–95.
- [26] H. Herger, R. Roth, The Unitary Correlation Operator Method from a Similarity Renormalization Group Perspective, *Phys. Rev. C* 75 (2007) 051001.
- [27] R. Roth, S. Reinhardt, H. Herger, Unitary Correlation Operator Method and Similarity Renormalization Group: Connections and Differences, *Phys. Rev. C* 77 (2008) 064003.
- [28] E. Anderson, et al., Block Diagonalization using SRG Flow Equations, *Phys. Rev. C* 77 (2008) 037001.
- [29] D. R. Entem, R. Machleidt, Accurate Charge-Dependent Nucleon-Nucleon Potential at Fourth Order of Chiral Perturbation Theory, *Phys. Rev. C* 68 (2003) 041001.
- [30] E. L. Gubankova, F. Wegner, Modified similarity renormalization of Hamiltonians: Positronium on the light front.
- [31] E. L. Gubankova, F. Wegner, Flow equations for QED in the light front dynamics, *Phys. Rev. D* 58 (1998) 025012.
- [32] A. Akmal, V. R. Pandharipande, D. G. Ravenhall, The equation of state for nucleon matter and neutron star structure, *Phys. Rev. C* 58 (1998) 1804–1828.
- [33] K. Hebeler, S. Bogner, R. Furnstahl, A. Nogga, A. Schwenk, Improved nuclear matter calculations from chiral low-momentum

- interactions, Phys. Rev. C 83 (2011) 031301.
- [34] H. A. Bethe, Theory of nuclear matter, Ann. Rev. Nucl. Part. Sci. 21 (1971) 93–244.
- [35] B. M. Axilrod, E. Teller, J. Chem. Phys. 11 (1943) 299.
- [36] R. J. Bell, I. J. Zucker, Long-Range Forces, in: M. L. Klein, J. A. Venables (Eds.), Rare Gas Solids, Vol. 1, Academic Press, London, 122–175, 1976.
- [37] K. Hebeler, Private communication.
- [38] E. D. Jurgenson, R. J. Furnstahl, Similarity Renormalization Group Evolution of Many-Body Forces in a One-Dimensional Model, Nucl. Phys. A 818 (2009) 152–173.
- [39] P. Navratil, G. P. Kamuntavicius, B. R. Barrett, Few-nucleon systems in translationally invariant harmonic oscillator basis, Phys. Rev. C 61 (2000) 044001.
- [40] A. Nogga, H. Kamada, W. Glöckle, Modern nuclear force predictions for the alpha particle, Phys. Rev. Lett. 85 (2000) 944–947.
- [41] R. Roth, S. Binder, K. Vobig, A. Calci, J. Langhammer, et al., Ab Initio Calculations of Medium-Mass Nuclei with Normal-Ordered Chiral NN+3N Interactions .
- [42] S.R. Beane et al., “From Hadrons to Nuclei: Crossing the Border”, At the Frontier of Particle Physics, Ed. M. Shifman, Vol. 1, p. 133, World Scientific, arXiv:nucl-th/0008064, 2000.
- [43] E. Epelbaum, H.-W. Hammer, U.-G. Meissner, Modern Theory of Nuclear Forces, Rev. Mod. Phys. 81 (2009) 1773–1825.
- [44] S. R. Beane, P. F. Bedaque, M. J. Savage, U. van Kolck, Towards a perturbative theory of nuclear forces, Nucl. Phys. A 700 (2002) 377–402.
- [45] P. F. Bedaque, U. van Kolck, Effective field theory for few-nucleon systems, Ann. Rev. Nucl. Part. Sci. 52 (2002) 339–396.
- [46] A. Nogga, R. G. E. Timmermans, U. van Kolck, Renormalization of One-Pion Exchange and Power Counting, Phys. Rev. C 72 (2005) 054006.
- [47] S. K. Bogner, R. J. Furnstahl, S. Ramanan, A. Schwenk, Convergence of the Born Series with Low-Momentum Interactions, Nucl. Phys. A 773 (2006) 203–220.
- [48] S. Weinberg, Quasiparticles and the Born Series, Phys. Rev. 131 (1963) 440–460.
- [49] S. Ramanan, S. K. Bogner, R. J. Furnstahl, Weinberg Eigenvalues and Pairing with Low-Momentum Potentials, Nucl. Phys. A 797 (2007) 81–93.
- [50] S. K. Bogner, A. Schwenk, R. J. Furnstahl, A. Nogga, Is nuclear matter perturbative with low-momentum interactions?, Nucl. Phys. A 763 (2005) 59–79.
- [51] E. Epelbaum, W. Glöckle, U.-G. Meissner, The two-nucleon system at next-to-next-to-next-to-leading order, Nucl. Phys. A 747 (2005) 362–424.
- [52] E. Anderson, S. Bogner, R. Furnstahl, R. Perry, Operator Evolution via the Similarity Renormalization Group I: The Deuteron, Phys. Rev. C 82 (2010) 054001.
- [53] E. Anderson, Private communication.
- [54] A. L. Fetter, J. D. Walecka, Quantum Many-Particle Systems, McGraw-Hill, New York, 1972.
- [55] P. Ring, P. Schuck, The Nuclear Many-Body Problem, Springer, Berlin, 2005.
- [56] J. W. Negele, H. Orland, Quantum Many-Particle Systems, Addison-Wesley, Redwood City, CA, 1988.
- [57] K. Tsukiyama, S. Bogner, A. Schwenk, In-Medium Similarity Renormalization Group for Nuclei, Phys. Rev. Lett. 106 (2011) 222502.
- [58] P. Maris, J. Vary, P. Navratil, W. Ormand, H. Nam, et al., Origin of the anomalous long lifetime of  $^{14}\text{C}$ , Phys. Rev. Lett. 106 (2011) 202502.
- [59] P. Maris, A. Shirokov, J. Vary, Ab initio nuclear structure simulations: The Speculative  $^{14}\text{F}$  nucleus, Phys. Rev. C 81 (2010) 021301.
- [60] V. Goldberg, B. Roeder, G. Rogachev, G. Chubarian, E. Johnson, et al., First observation of  $^{14}\text{F}$ , Phys. Lett. B692 (2010) 307–311.
- [61] P. Navratil, S. Quaglioni, R. Roth, Ab Initio Theory of Light-ion Reactions, J.Phys.Conf.Ser. 312 (2011) 082002.
- [62] P. Navratil, R. Roth, S. Quaglioni, Ab initio many-body calculations of nucleon scattering on  $^4\text{He}$ ,  $^7\text{Li}$ ,  $^7\text{Be}$ ,  $^{12}\text{C}$  and  $^{16}\text{O}$ , Phys. Rev. C 82 (2010) 034609.
- [63] P. Navratil, R. Roth, S. Quaglioni, Ab initio many-body calculation of the  $^{7}\text{Be}(\text{p},\gamma)^{8}\text{B}$  radiative capture, Phys. Lett. B704 (2011) 379–383.
- [64] G. Hagen, T. Papenbrock, D. J. Dean, M. Hjorth-Jensen, Medium-mass nuclei from chiral nucleon-nucleon interactions, Phys. Rev. Lett. 101 (2008) 092502.
- [65] G. Hagen, T. Papenbrock, D. Dean, M. Hjorth-Jensen, Ab initio coupled-cluster approach to nuclear structure with modern nucleon-nucleon interactions, Phys. Rev. C 82 (2010) 034330.
- [66] G. Hagen, T. Papenbrock, M. Hjorth-Jensen, Ab Initio Computation of the  $^{17}\text{F}$  Proton Halo State and Resonances in  $\text{A}=17$  Nuclei, Phys. Rev. Lett. 104 (2010) 182501.
- [67] T. Otsuka, T. Suzuki, J. D. Holt, A. Schwenk, Y. Akaishi, Three-body forces and the limit of oxygen isotopes, Phys. Rev. Lett. 105 (2010) 032501.
- [68] H. Hergert, R. Roth, Private communication.
- [69] K. Hebeler, A. Schwenk, Chiral three-nucleon forces and neutron matter, Phys. Rev. C 82 (2010) 014314.
- [70] K. Hebeler, J. Lattimer, C. Pethick, A. Schwenk, Constraints on neutron star radii based on chiral effective field theory interactions, Phys. Rev. Lett. 105 (2010) 161102.
- [71] M. Stoitsov, M. Kortelainen, S. Bogner, T. Duguet, R. Furnstahl, et al., Microscopically-based energy density functionals for nuclei using the density matrix expansion: Implementation and pre-optimization, Phys. Rev. C 82 (2010) 054307.
- [72] S. Bogner, R. Furnstahl, H. Hergert, M. Kortelainen, P. Maris, et al., Testing the density matrix expansion against ab initio calculations of trapped neutron drops, Phys. Rev. C 84 (2011) 044306.